A mouse model of PTEN Hamartoma Tumour Syndrome reveals that loss of the nuclear function of PTEN drives macrocephaly, lymphoid overgrowth, and late-onset cancer

Priyanka Tibarewal[1,*], Victoria Rathbone[1], Sarah E Conduit[1], Gala Anastasia Electra Classen[1], Fiona Black[1], Mohammad Amin Danesh[1], Georgia Constantinou[1], Zeinab Asgarian[2], Koujiro Tohyama[3], Nisha Kriplani[4], Virginia Alvarez Garcia[4], Elizabeth Foxall[1], Djenat Belarbi[5,6,7], Marie Leverve[5,6,7], Wayne Pearce[1], Mahreen Adil[1], Zofia Varyova[1], Lucia Conde[1], Adriana Alves[1], Glenn R Masson[8], Roger L Williams[8], Adrienne M Flanagan[9, 10], Javier Herrero[1], , Katerina Stroud[11], Marc Tischkowitz[11], Katherine Lachlan[12,13], Cheryl L Scudamore[14], Mark G H Scott[5,6,7], Nicholas R Leslie[4], Nicoletta Kessaris[2,*], Bart Vanhaesebroeck[1,*]

[1]Cancer Institute, University College London, UK
[2]Wolfson Institute of Biomedical Research, University College London, UK
[3]Department of Physiology, School of Dentistry, Iwate Medical University, Yahaba, Japan
[4]Institute of Biological Chemistry, Biophysics and Bioengineering, Heriot Watt University, Edinburgh, UK
[5]Université de Paris, 75014 Paris, France
[6]Institut Cochin, INSERM U1016, 75014 Paris, France
[7]CNRS, UMR8104, 75014 Paris, France
[8]MRC Laboratory of Molecular Biology, Cambridge, UK
[9]Research Department of Pathology, University College London, UK
[10]Cellular and Molecular Pathology, Royal National Orthopaedic Hospital, Stanmore, UK
[11]Department of Genomic Medicine, National Institute for Health Research Cambridge Biomedical Research Centre, University of Cambridge, Cambridge, UK
[12]Wessex Clinical Genetics Service, University Hospital Southampton, Princess Anne Hospital, Southampton, UK
[13]Human Development and Health, Faculty of Medicine, University of Southampton, Southampton, UK
[14]Exepathology, Exmouth, UK

*Corresponding authors

Author contributions: PT, NRL, NK and BV conceived the study, PT, VR, SEC, GAEC, FB, MAD, GC, ZA,KT, NK, VAG, EF, DB, ML,WP, MA, ZV, SH, LC, AA, GRM and MGHS performed and analysed the experiments, CLS performed the histological analysis, RLW, AMF and JH provided reagents/resources for the study, PT, NK and BV wrote the manuscript.

Competing interest statement: BV is a consultant for Pharming (Leiden, The Netherlands) and iOnctura (Geneva, Switzerland) and a shareholder of Open Orphan (Dublin, Ireland).

ABSTRACT

PTEN Hamartoma Tumour Syndrome (PHTS) is a rare disorder characterized by germline heterozygous mutations in the PTEN tumour suppressor gene, leading to multi-organ/tissue overgrowth, autism spectrum disorder and increased cancer risk. PHTS individuals display heterogeneity in phenotypes, which has been linked in part to the diverse genetic alterations in the *PTEN* gene and the multifaceted functions of this protein. Indeed, while PTEN primarily functions as a PIP_3 lipid phosphatase in the cytosol, regulating PI3K/AKT signalling, a pathway commonly

deregulated in cancer, it also plays crucial roles in maintaining chromosomal stability through nuclear activities such as double strand (ds) DNA damage repair. Recent studies have identified a subset of missense PHTS variants that cause nuclear exclusion of PTEN, impairing its nuclear functions. Here, we present our findings from one such pathogenic variant, *PTEN-R173C*, frequently found in PHTS and somatic cancers. Using cell biological and mouse modelling approaches, we show that PTEN-R173C has higher PIP_3 phosphatase activity than wild-type PTEN, resulting in effective regulation of canonical PI3K/AKT signalling. However, PTEN-R173C is unstable and excluded from the nucleus. Aligning with their near normal PI3K/AKT signalling, *Pten*$^{+/R173C}$ mice display a low incidence of solid tumours compared to *Pten*$^{+/-}$ mice. *Pten*$^{+/R173C}$ mice also exhibit lymphoid hyperplasia and macrocephaly which correlates with compromised nuclear functions of PTEN-R173C. That nuclear functions are compromised is demonstrated by reduced dsDNA damage repair in *Pten*$^{+/R173C}$ mice. Integrating PHTS patient data with findings from our mouse model, our study indicates that nuclear dysfunction of pathogenic *PTEN* variants is a key factor in predicting the onset of the different PHTS-associated phenotypes. We speculate that late-onset cancer in individuals with nuclear-excluded PTEN results from genetic alterations unrelated to PTEN itself, facilitated by impaired PTEN-mediated dsDNA damage repair.

KEY WORDS: PTEN, PI3K, PHTS, overgrowth, mouse model, cancer, macrocephaly, germline, ASD

INTRODUCTION

PTEN is a ubiquitously expressed tumour suppressor (Alvarez-Garcia et al., 2019, Li et al., 1997, Steck et al., 1997) that shows complete loss of expression in some cancers (e.g. prostate cancer and glioblastoma) and overrepresentation of missense variants in other tumours (e.g. endometrial cancer) (Alvarez-Garcia et al., 2019, Yehia et al., 2020). Heterozygous germline variants in PTEN cause PTEN Hamartoma Tumour Syndrome (PHTS), a rare autosomal dominant disorder. A recent study puts the prevalence of PHTS as 1:8000-13,000 (White et al., 2025) which is 10-20 fold higher than previous estimates (Nelen et al., 1996). Clinical features of PHTS include macrocephaly, developmental delay (DD), autism spectrum disorder (ASD), dermatological pathologies, gastrointestinal (GI) polyps, immune dysfunction, vascular anomalies. Individuals with PHTS also face a significantly increased risk of developing cancers particularly of the breast, endometrium and thyroid (Ngeow and Eng, 2019, Yehia and Eng, 2018), with emerging evidence for ovarian cancer (Schei-Andersen et al., 2025).

PTEN acts in both the cytosol and nucleus. Cytosolic functions of PTEN predominantly include lipid phosphatase activity on phosphatidylinositol(3,4,5)trisphosphate (PIP_3) and phosphatidylinositol(3,4)bisphosphate ($PI(3,4)P_2$), thereby antagonizing PI3K/AKT signalling (Myers et al., 1998). PTEN also has protein-phosphatase activity, reducing phosphorylation of Ser/Thr/Tyr on proteins such as PTK6, DREBRIN, DVL2, FAK and SHC (Leslie et al., 2009) , in addition to auto-dephosphorylating its T366 site (Tibarewal et al., 2012). Nuclear PTEN has been implicated in cell cycle control, dsDNA repair, maintenance of chromatin structure, genome integrity and transcriptional control (Ho et al., 2019, Langdon, 2023).

The functional core of the PTEN protein consists of a catalytic (amino acids (AA) 16-185) and a C2 (AA 186-350) domain (Lee et al., 1999), with mutations in different regions differentially impacting PTEN expression and function. 65% of PHTS patients express *PTEN* variants such as deletions, DNA insertions or non-sense mutation leading to STOP codons (such as R130X and R233X) that result in PTEN truncation and are therefore predicted to cause heterozygous loss-of-expression. The remaining PHTS patients carry heterozygous missense mutations in the phosphatase or C2 domain, leading to expression of PTEN proteins with altered function or subcellular distribution (Hendricks et al., 2022,

95 Spinelli et al., 2015). These include mutations in the catalytic pocket resulting in loss of all catalytic
96 activity [e.g. C124 (C124S/R), R130 (R130G/Q/L) and G129 (G129R)] (Lee et al., 1999) or selective loss
97 of PIP_3 phosphatase activity, while retaining protein phosphatase activity (e.g. G129E) (Myers et al.,
98 1998). Missense mutations leading to selective loss of protein phosphatase activity (Y138L/C) have
99 also been described, although these have not been reported in PHTS (Davidson et al., 2010, Tibarewal
100 et al., 2012). Recent reports have shown that a subset of PTEN variants in PHTS (including K289E,
101 D252G, F241S, I101T and others) are excluded from the nucleus and therefore lack all PTEN nuclear
102 functions (Langdon, 2023).
103 The PIP_3 phosphatase activity of PTEN has long been regarded as the main and critical factor in
104 PHTS pathogenesis, yet other lipid phosphatase-independent functions of PTEN are now also emerging
105 as important (Langdon, 2023). Various studies have attempted to establish genotype-phenotype
106 associations in PHTS. Limited patient data make it challenging to ascertain the impact of individual
107 variants in driving patient phenotypes. This challenge has been partially overcome by classifying the
108 variants based on their position in the *PTEN* gene and their impact on PTEN expression and function
109 (Lachlan et al., 2007, Leslie and Longy, 2016, Marsh et al., 1998, Marsh et al., 1999, Mighell et al.,
110 2018). Recently, a large paediatric and adult patient cohort study revealed that missense variants are
111 associated with early disease onset, with DD and macrocephaly being the reason for early diagnosis,
112 whereas *PTEN* truncation variants are associated with late onset disease, with cancer being the reason
113 for PHTS diagnosis at later stages in life (Hendricks et al., 2022). However, patient cohort studies have
114 been limited by the variability in age and sex of the individuals, one of the key challenges in rare disease
115 research.
116 Genetically modified mice have helped overcome some of the challenges in PTEN research by
117 allowing assessment of PTEN functions in an endogenous tissue context (Lee and Pandolfi, 2020). They
118 also serve as a platform for testing potential treatments, such as PI3K pathway inhibitors, aimed at
119 mitigating the effects of PTEN loss. An example are mice with heterozygous loss of PTEN expression
120 (*Pten*$^{+/-}$), representing *PTEN* variants that result in loss of expression and function. This mouse model
121 recapitulates many aspects of human PHTS remarkably well in terms of cancer development and
122 lymphoid and brain overgrowth (Podsypanina et al., 1999, Tibarewal et al., 2022).
123 Here we report the creation and characterisation of a novel mouse model for PHTS, carrying a
124 PTEN-R173C (NM_000314.8(PTEN):c.517C>T (p.Arg173Cys)) missense variant in the germline. R173 is
125 located in the TI (Thr-Ile) loop in the catalytic domain of PTEN important for PTEN catalytic activity (Lee
126 et al., 1999). Mutation of R173 to Cys or His in similar ratios are observed in PHTS and sporadic cancers,
127 with conflicting reports on catalytic activity impact, from having been reported active to inactive (Han
128 et al., 2000, Post et al., 2020, Smith and Briggs, 2016). R173 variants are frequently found in multiple
129 patient cohort studies with 34 PHTS patients been reported in literature to the best of our knowledge,
130 and an additional four new patients identified with this variant in the UK (**Supplementary Table 1**).
131 Most patients with R173 variants received PHTS diagnosis at young age due to presentation of
132 macrocephaly, DD and cutaneous pathology. Adult patients additionally presented with breast cancer,
133 benign and malignant tumours of the skin, thyroid and ovary, endometrial polyps and fibroids, GI
134 polyps, with malignant disease onset much later in life (over the age of 50 years). Vascular
135 malformations, mainly haemangiomas, were also seen in adult patients (**Table 1** and **Supplementary**
136 **Table 1**).
137 Here, we first revisited the impact of the R173 mutation on PTEN expression and function using
138 biochemical and cell-based models, with a focus on PTEN-R173C. We show that PTEN-R173C has
139 reduced protein stability but retains its ability to dephosphorylate PIP_3 and therefore regulate the
140 canonical PI3K/AKT pathway in the cytosol. However, we find that this PTEN mutant is largely excluded
141 from the nucleus.

142 Several mouse models have been developed to distinguish the relative importance of the cytosolic
143 *versus* nuclear functions of PTEN (reviewed in (Langdon, 2023)). For instance, *Pten*^{m3m4} mice,
144 engineered by Eng *et al.*, feature non-naturally occurring PTEN mutations that result in a
145 predominantly cytosolic PTEN distribution without affecting its PIP_3 phosphatase activity. These mice
146 have been extensively studied for the impact of the nuclear-cytoplasmic partitioning of PTEN on
147 neuronal and immune phenotypes, although their tumour spectrum has not been reported (Mester
148 et al., 2011, Tilot et al., 2014, Jaini et al., 2020). Other models, expressing PTEN missense variants
149 found in PHTS such as F341V (Caserta et al., 2015), and non-pathogenic mutations such as K13R, Y240F
150 and D384V (Igarashi et al., 2018, Ma et al., 2019), that do not affect the catalytic functions of PTEN but
151 impact its nuclear/sub-cellular localisation, have also been developed, but there is limited or no
152 patient data for these individual variants (**Table 1** and **Supplementary Table 2**).
153 We created heterozygous germline *Pten*^{R173C} knock-in mice (*Pten*$^{+/R173C}$) as a unique model of a
154 frequent pathogenic PHTS PTEN variant representing nuclear-excluded PTEN missense variants. We
155 examined the consequences of this mutation on embryonic development, glucose metabolism,
156 development of PHTS-relevant cancers as well as immune, neurological and behavioural phenotypes.
157 By integrating our findings with phenotypic data from patients for this variant, and by comparison of
158 reported data on the *Pten*^{m3m4} mice, we delineate the role of the nuclear functions of PTEN in the
159 manifestation of PHTS phenotypes.
160
161 **RESULTS**
162 **Increased PIP_3 phosphatase activity but reduced protein stability of PTEN-R173 mutant proteins**
163 **upon transient expression in mammalian cells**
164 Conflicting data on the catalytic activity of PTEN-R173 variants have been published. PTEN-R173
165 mutant proteins, expressed in *E. coli*, have been reported to be catalytically inactive (Han et al., 2000)
166 however, mutant PTEN proteins expressed in non-mammalian systems often fail to fold properly,
167 resulting in lack of activity (Spinelli et al., 2015). Consistent with this, in our hands, PTEN-R173C protein
168 expressed in *E. coli* lacked *in vitro* PIP_3 lipid phosphatase activity (**Fig. S1**) and when expressed in Sf9
169 insect cells precipitated upon purification (Masson et al., 2016a) (data not shown), rendering it
170 unsuitable for use in *in vitro* assays.
171 A commonly used assay to determine the ability of PTEN and its mutants to regulate PI3K/AKT
172 signalling involves transfection into the PTEN-null U-87 MG glioblastoma cell line (further referred to
173 as U87) and assessment of basal AKT phosphorylation and cell proliferation (Davidson et al., 2010).
174 Transient lentiviral expression of untagged PTEN-R173C in U87 revealed consistently lower expression
175 levels compared to PTEN-WT (**Fig. 1A**, left panel), despite similar mRNA expression levels (**Fig. 1A**, right
176 panel). Similar results were seen with PTEN-R173H, suggesting that other PTEN-R173 mutant proteins
177 are less stable than PTEN-WT.
178 Expression of a dose range of PTEN proteins in U87 revealed that, compared to PTEN-WT, lower
179 levels of PTEN-R173C or PTEN-R173H effectively downregulated AKT P-S473 and S6 P-S240/244
180 phosphorylation (**Fig. 1B**) and suppressed U87 proliferation (**Fig. 1C and S2A**). We also assessed the
181 impact of PTEN-R173C expression in U87 cells on recruitment of a PIP_3-biosensor protein to the plasma
182 membrane. In both serum-starved or insulin-stimulated cells, the biosensor plasma membrane to
183 cytosol ratio (PM:cytosol) was significantly reduced upon treatment with the pan-class I PI3K inhibitor
184 GDC-0941 or upon expression of PTEN-WT or PTEN-R173C, with the strongest decrease upon PTEN-
185 R173C expression (**Fig. 1D and S2B**), despite its lower expression levels compared to PTEN-WT (**Fig.**
186 **S2C**).
187 Taken together, these data suggest that in mammalian cells, PTEN-R173C is less stable but
188 catalytically more active than PTEN-WT.
189
190 **Evidence for a more open, proteolytically-sensitive protein conformation of PTEN-R173 mutants**
191 We next investigated possible biochemical mechanisms underlying the reduced expression of PTEN-
192 R173C mutants in U87 cells. Cycloheximide chase experiments of U87 cells transiently transfected with

193 PTEN expression constructs indicated a reduced protein half-life of PTEN-R173C compared to PTEN-
194 WT (**Fig. 1E, S3A** and Ref.(Spinelli et al., 2015)). A recent study has shown similar findings with PTEN-
195 R173H (Jun et al., 2024).
196 PTEN protein stability and activity is regulated, in part, by phosphorylation on multiple C-terminal
197 sites (S380/T382/T383/S385) by kinases such as CK2 (Torres and Pulido, 2001). Such phosphorylation
198 results in a more closed, less active and more stable protein conformation (Torres and Pulido, 2001,
199 Vazquez et al., 2001, Birle et al., 2002, Odriozola et al., 2007, Dempsey et al., 2021). Upon transient
200 expression of similar levels of untagged proteins in U87 cells, PTEN-R173C showed a ~50% lower level
201 of S380/T382/T383 phosphorylation compared to PTEN-WT (**Fig. 1F**). Similar data were observed using
202 YFP-tagged Rluc-PTEN-R173C and PTEN-R173H in HEK-293T cells (**Fig. S3B**), suggesting that reduced
203 phosphorylation may contribute to the observed instability of PTEN-R173 mutants.
204 Dephosphorylation of S380/T382/T383/S385 on PTEN releases the inhibitory effect of these
205 phosphorylated residues on the C2 domain of PTEN, leading to a more open conformation with
206 increased membrane binding and therefore enhanced activity (Torres and Pulido, 2001, Vazquez et
207 al., 2001, Birle et al., 2002, Odriozola et al., 2007). It has also been shown that, once at the membrane,
208 the active form of PTEN becomes degraded (Maccario et al., 2010). A study using computational
209 modelling predicted increased protein flexibility of PTEN-R173C/H mutants, leading to impaired
210 protein stability (Smith and Briggs, 2016). In order to gain insight into these phenomena, we used an
211 intramolecular bioluminescent resonance energy transfer (BRET)-based biosensor Rluc-PTEN-YFP in
212 live HEK-293T and PTEN KO HeLa cells. This biosensor reveals dynamic changes in PTEN conformational
213 rearrangement and function due to shifts in energy transfer between the donor/acceptor couple
214 (Lima-Fernandes et al., 2014) (**Fig. S4A-B**). Using this approach, PTEN-R173C and PTEN-R173H were
215 found to be in a more open/flexible conformation compared to PTEN-WT (**Fig. 1G**).
216 We previously reported that PTEN protein dephosphorylated on S380/T382/T383/S385 is more
217 prone to ubiquitination and degradation, and that this involves the K66 ubiquitination site in PTEN
218 (Maccario et al., 2010, Gupta and Leslie, 2016). In line with this, when transiently expressed in U87
219 cells, the PTEN-R173C/K66R double mutant which cannot be ubiquitinylated, showed increased
220 protein expression levels compared to PTEN-R173C (**Fig. 1H**).
221 Altogether these data indicate that the PTEN-R173C protein has a more open conformation that
222 allows ubiquitination and degradation, leading to reduced protein levels.
223
224 **PTEN-R173 mutants are predominantly cytoplasmic and largely excluded from the nucleus**
225 The tumour suppressor functions of PTEN have been mostly attributed to its ability to regulate the
226 PI3K/AKT pathway, with the role of other PTEN functions such as protein phosphatase activity and
227 nuclear functions less well-studied in this context (Ho et al., 2019). Given that our results so far show
228 that PTEN-R173C/H mutants are effective at regulating the PI3K/AKT pathway, we turned our
229 attention to other PTEN functions that might explain the high mutation frequency of this site in
230 somatic cancers and PHTS.
231 Analysis of the subcellular distribution of PTEN-R173C by transiently expressing C-terminally GFP-
232 tagged PTEN-R173C or PTEN-WT in Lenti-X™ 293T cells revealed a significantly lower
233 nuclear:cytoplasmic ratio of the GFP signal in cells expressing PTEN-R173C-GFP than in cells with PTEN-
234 WT-GFP, suggesting that PTEN-R173C was largely excluded from the nucleus (**Fig. 1I**). Nuclear
235 exclusion of the R173 mutants was also revealed upon expression of YFP-tagged Rluc-PTEN-WT, -
236 R173C or -R173H in HEK-293T or PTEN KO HeLa cells (**Fig. S5**).
237
238 **Homozygous germline PTEN-R173C expression is embryonically lethal in mice**
239 In order to study PTEN-R173C in its endogenous tissue context and to better understand its role in
240 PHTS, we created heterozygous germline *Pten*^{R173C} knock-in mice (*Pten*$^{+/R173C}$) by CRISPR-Cas9
241 technology (**Fig. S6**). Intercrosses of *Pten*$^{+/R173C}$ mice did not yield live-born homozygous *Pten*$^{R173C/R173C}$
242 mice (**Fig. 2A**). *Pten*$^{R173C/R173C}$ embryos were almost all reabsorbed at embryonic day (E)11.5, with
243 under-representation compared to Mendelian ratios at earlier time points (**Fig. 2A**). Intact

244 *Pten*$^{R173C/R173C}$ embryos were found up to E9.5 at which stage, 5 out of 9 embryos were smaller and had
245 not undergone turning, with the remaining 4 having been reabsorbed, suggesting that *Pten*$^{R173C/R173C}$
246 embryos die around E9.5 (**Fig. 2A**).
247 Given the embryonic lethality of homozygous *Pten* $^{R173C/R173C}$ mice, and the notion that PTEN
248 mutations in PHTS individuals are heterozygous, in the next series of experiments we used
249 heterozygous *Pten*$^{+/R173C}$ mice to further investigate the impact of the PTEN R173C mutation. For these
250 studies, we used littermate wild-type (*Pten*$^{+/+}$) mice as controls as well as *Pten*$^{+/-}$ mice, a well-
251 characterised model for PHTS (Knobbe et al., 2008, Di Cristofano et al., 1998, Suzuki et al., 1998,
252 Podsypanina et al., 1999, Freeman et al., 2006, Di Cristofano et al., 2001).
253
254 **PTEN-R173C expressed from its endogenous promoter is unstable but retains PIP_3 phosphatase**
255 **activity**
256 As a cell-based model to study endogenous PTEN-R173C protein expression and function, we derived
257 mouse embryonic fibroblasts (MEFs) of the following genotypes: *Pten*$^{+/R173C}$, *Pten*$^{R173C/R173C}$, *Pten*$^{-/R173C}$
258 and compared these to *Pten*$^{+/-}$, *Pten*$^{-/-}$ and *Pten*$^{+/+}$ MEFs.
259 PTEN protein expression levels in *Pten*$^{+/R173C}$ and *Pten*$^{+/-}$ MEFs were 60-70% of those in *Pten*$^{+/+}$ MEFs
260 (**Fig. 2B**). The PTEN levels observed in *Pten*$^{+/-}$ MEFs agree with previous studies where the *Pten*^{WT} allele
261 was shown to express higher than 50% level of PTEN protein (Alimonti et al., 2010). In *Pten*$^{R173C/R173C}$
262 and *Pten*$^{-/R173C}$ MEFs, PTEN protein levels were ~13% and ~2%, respectively, of those in *Pten*$^{+/+}$ MEFs
263 (**Fig. 2C**; **Fig. S7**), indicative of low protein stability of the PTEN-R173C protein, in line with our
264 exogenous expression studies above.
265 We next used immunoblotting to assess PI3K pathway activation, under standard cell culture
266 conditions and upon insulin-stimulation. *Pten*$^{+/R173C}$, *Pten*$^{+/-}$ and *Pten*$^{+/+}$ MEFs growing in complete
267 media showed similar basal levels of phosphorylation of AKT, S6 and other downstream effectors (**Fig.**
268 **2B**). Under these conditions, *Pten*$^{-/-}$ MEFs had increased levels of AKT P-S473, which was not observed
269 in *Pten*$^{R173C/R173C}$ MEFs (**Fig. 2C**). In *Pten*$^{-/R173C}$ MEFs, the levels of AKT P-S473 were elevated compared
270 to *Pten*$^{+/+}$ and *Pten*$^{+/-}$ MEFs, but still substantially lower compared to *Pten*$^{-/-}$ MEFs (**Fig. S7**).
271 Upon insulin stimulation, the increase in AKT P-S473 was dampened more effectively in
272 *Pten*$^{R173C/R173C}$ MEFs than in *Pten*$^{+/+}$ and *Pten*$^{-/-}$ MEFs, despite the very low levels of PTEN-R173C
273 expression (**Fig. 2D**).
274 Taken together, these data indicate that, even at low levels of expression, PTEN-R173C is still
275 capable of effectively downregulating unstimulated and insulin-stimulated AKT P-S473
276 phosphorylation and thus retains overall PIP_3 phosphatase activity.
277
278 **PTEN-R173C regulates glucose metabolism *in vivo***
279 PTEN plays an important role in glucose metabolism by dampening insulin signalling, with *Pten*$^{+/-}$ mice
280 showing enhanced acute insulin signalling and increased glucose metabolism (Chen et al., 2018,
281 Garcia-Cao et al., 2012, Pal et al., 2012). PHTS patients also often show constitutive insulin sensitization
282 (Pal et al., 2012). In line with these reports, insulin tolerance tests on 3-month-old mice revealed
283 enhanced insulin sensitivity in *Pten*$^{+/-}$ mice, evidenced by lower levels of blood glucose post insulin
284 injection compared to WT littermates (**Fig. 2E**). In contrast, WT and *Pten*$^{+/R173C}$ mice showed a similar
285 insulin response up to 60 min after insulin injection (**Fig. 2E**). This indicates that, at the organismal
286 level, PTEN-R173C maintains the ability to downregulate acute insulin/PI3K/AKT signalling and
287 therefore glucose homeostasis (**Fig. 2E**).
288
289 **PTEN-R173C expressed from an endogenous promoter is predominantly nuclear-excluded with**
290 **reduced ability to regulate dsDNA damage repair**
291 To determine the subcellular distribution of PTEN-R173C upon expression from its endogenous locus,
292 we used immunocytochemistry and quantification of the PTEN nuclear/cytoplasmic ratio in
293 *Pten*$^{R173C/R173C}$ and *Pten*$^{-/R173C}$ MEFs. These data showed that PTEN-R173C expressed from its
294 endogenous locus was predominantly nuclear-excluded, in contrast to PTEN-WT protein which was

295 present in both the nucleus and cytoplasm (**Fig. 2F and S8A**). Given that R173 is not located in a known
296 PTEN nuclear localisation signal, one reason for the apparent nuclear exclusion of PTEN-R173C could
297 be sequestration at the plasma membrane, with little protein available for nuclear import. To
298 investigate this, we treated *Pten*$^{R173C/R173C}$ MEFs with the pan-class I PI3K inhibitor GDC-0941, with the
299 aim to reduce the PIP_3 substrate levels for PTEN at the plasma membrane and to potentially restore
300 the presence of PTEN-R173C in the nucleus. However, GDC-0941 treatment did not affect the
301 subcellular distribution of PTEN-R173C (**Fig. S8B**), suggesting that plasma membrane PIP_3 levels do not
302 significantly contribute to the nuclear exclusion of PTEN-R173C.
303 Nuclear PTEN has numerous functions including regulation of DNA repair, transcription, chromatin
304 structure, chromosomal stability and genome integrity by various mechanisms (Ho et al., 2019,
305 Langdon, 2023). We investigated one of these nuclear functions in *Pten*$^{+/R173C}$ mice, namely dsDNA
306 repair. Nuclear PTEN deficiency has been shown to cause a homologous recombination (HR) defect in
307 cells, leading to increased γH2AX expression and decreased Rad51 foci formation upon genotoxic
308 stress such as ionizing radiation (Bassi et al., 2013, Mendes-Pereira et al., 2009, Shen et al., 2007).
309 Ionizing radiation (IR) of *Pten*$^{+/R173C}$ and *Pten*$^{+/-}$ mice, followed by analysis 5 h post-IR treatment, led to
310 a similar increase in γH2AX levels in protein extracts from uteri, kidney and liver, compared to wild-
311 type mice (**Fig. 2G and S9**), indicative of a similarly reduced DNA repair capacity upon heterozygous
312 PTEN loss or heterozygous PTEN-R173C expression. This suggests that PTEN-R173C has a reduced
313 ability to regulate DNA damage repair compared to PTEN-WT.
314
315 **Reduced cancer predisposition of *Pten*$^{+/R173C}$ mice compared to *Pten*$^{+/-}$ mice**
316 Individuals with PHTS have an increased risk of cancers of multiple tissues including breast,
317 endometrium and thyroid (Yehia and Eng, 2018, Yehia et al., 2020, Yehia et al., 2019). To gain insight
318 into the cancer predisposition of germline *Pten*^{R173C} expression, we aged heterozygous *Pten*$^{+/R173C}$ mice
319 alongside *Pten*$^{+/-}$ and *Pten*$^{+/+}$ littermate controls. We used mice on a mixed C57Bl/6JxSv129
320 background, as on this background *Pten*$^{+/-}$ mice develop PHTS-relevant phenotypes, with an
321 overlapping tumour spectrum including hyperplasia/tumours of the thyroid, endometrium, lymphoid
322 tissue, small intestine and adenomyoepithelioma and malignant mammary tumours in the females
323 (Tibarewal et al., 2022). *Pten*$^{+/-}$ mice also develop lesions not seen in PHTS patients including,
324 pheochromocytoma and intraepithelial neoplasia (PIN) and adenocarcinoma of the prostate (Knobbe
325 et al., 2008, Di Cristofano et al., 1998, Suzuki et al., 1998, Podsypanina et al., 1999, Freeman et al.,
326 2006, Di Cristofano et al., 2001).
327 Gross morphology and development of *Pten*$^{+/R173C}$ mice was found to be similar to *Pten*$^{+/+}$
328 littermates, with a tendency for a slight increase in body weight at young age in both *Pten*$^{+/R173C}$ and
329 *Pten*$^{+/-}$mice (**Fig. S10**).
330 Mice were aged and sacrificed at first appearance of signs of ill health or palpable masses. The
331 reasons for humane culling of mice are listed in **Supplementary Table 3**. Under these experimental
332 conditions, the median survival age of *Pten*$^{+/R173C}$ mice was 585 and 302 days for male and female mice,
333 respectively. This is significantly longer than the median survival age of 310 and 179 days for male and
334 female *Pten*$^{+/-}$ mice, respectively (**Fig.3A**). However, *Pten*$^{+/R173C}$ mice had a shorter lifespan compared
335 to wild-type mice (**Fig.3A**). This was especially the case for female *Pten*$^{+/R173C}$ mice, which were mainly
336 culled due to palpable masses or ill health.
337 Histopathological analysis of selected tissues from *Pten*$^{+/-}$ and *Pten*$^{+/R173C}$ mice revealed very similar
338 gross morphologies of all tissues analysed, with overall histopathology data summarized in **Fig. 3B** and
339 **Supplementary Tables 4-7.**
340 *Pten*$^{+/R173C}$ mice developed far fewer tumours than *Pten*$^{+/-}$ mice, with occasional hyperplasia of the
341 small intestine (2/14 mice) and low-grade PINs of prostate (4/14 mice), one case of mammary
342 adenocarcinoma (1/22 mice) and one case of endometrial hyperplasia (1/28) (**Fig. 3B; Fig. S11-S12;**
343 **Supplementary Tables 4 and 5**). Similar to *Pten*$^{+/-}$ mice, *Pten*$^{+/R173C}$ mice had a high incidence of
344 pheochromocytoma (**Fig. 3B, Fig. S11-S12; Supplementary Tables 4 and 5**).

345 One out of 28 *Pten*$^{+/R173C}$ mice displayed a single focus of endometrial hyperplasia, which correlated
346 with loss of immunostaining for PTEN and increased AKT P-S473 (**Fig. 3C**). Interestingly, loss of PTEN
347 immunoreactivity was also observed in microscopically *normal* endometrial glands from 5-month-old
348 and 10-month-old *Pten*$^{+/R173C}$ mice, but this was not accompanied by a concomitant increase in AKT P-
349 S473 immunoreactivity in these regions (**Fig. 3C**). In the absence of reagents which allow us to
350 specifically stain for WT or mutant PTEN protein and, based on the low expression level of endogenous
351 PTEN-R173C protein when expressed alone (**Fig. S7**), it is most likely that expression of the wild-type
352 *Pten* allele is lost in these morphologically normal glands. We speculate that, while the very low
353 expression level of PTEN-R173C from the endogenous allele may not be detectable by IHC, it is still
354 sufficient to partially downregulate PI3K signalling and AKT P-S473 and thereby prevent the
355 development of endometrial tumours. Although this observation is based on a single mouse, we
356 speculate that the hyperplastic gland found in the endometrium of this *Pten*$^{+/R173C}$ mouse may have
357 resulted either from loss-of-expression of the remaining *Pten*^{R173C} allele, or from acquisition of PI3K
358 pathway-activating mutations. These events likely led to PI3K pathway hyperactivation, ultimately
359 contributing to the development of endometrial hyperplasia. This hypothesis is supported by the fact
360 that somatic cancers with the PTEN-R173 mutation, along with mutation of the wild-type allele of
361 *PTEN*, also contain mutations in other cancer drivers such as *PIK3CA* (**Fig. 3D**).
362
363 **Prominent but delayed lymphoid hyperplasia in *Pten*$^{+/R173C}$ mice compared to *Pten*$^{+/-}$ mice**
364 Previous studies have reported a range of lymphoid and immune phenotypes in PHTS patients
365 including peripheral lymphoid hyperplasia, enlargement of tonsils and adenoids,
366 hypogammaglobulinemia, recurrent respiratory tract infection and autoimmune disorders. (Chen et
367 al., 2017, Drissen et al., 2024). Some of these phenotypes are found in a few PHTS patients with *PTEN-*
368 *R173* variants and other nuclear-excluded variants (**Table 1** and **Supplementary Tables 1&2**).
369 In *Pten* mutant mice, lymphoid hyperplasia leads to enlarged cervical, brachial, inguinal and axillary
370 lymph nodes (Podsypanina et al., 1999, Alimonti et al., 2010). While this does not cause discomfort to
371 the mice, in our study it was a main reason for sacrificing *Pten*$^{+/-}$ mice (75% males and 80% females)
372 and many *Pten*$^{+/R173C}$ mice (21% males and 50% females), due to animal welfare regulations on the
373 allowed tissue overgrowth size (**Supplementary Table 3**).
374 Histological analysis revealed a similar severity grade of hyperplasia (assessed by semi-quantitative
375 histopathological scoring) in female *Pten*$^{+/R173C}$ and *Pten*$^{+/-}$ mice but of significantly lower grade in
376 *Pten*$^{+/R173C}$ males than *Pten*$^{+/-}$ males (**Fig. 3E**). Lymphoid hyperplasia has also been reported in
377 heterozygous *Pten*$^{+/m3m4}$ mice (Jaini et al., 2020).
378 Flow cytometry analysis of lymph nodes of 5-month-old female *Pten*$^{+/-}$ and 10-month-old female
379 *Pten*$^{+/R173C}$ mice, the age at which they have visibly enlarged lymph nodes, compared to littermate
380 *Pten*$^{+/+}$ mice, revealed a significant increase in the proportion of B-cells and a corresponding decrease
381 in T-cell proportions, a phenotype also reported in *Pten*$^{+/m3m4}$ mice (**Fig. 3F-G**).
382 Although we did not assess dsDNA damage repair in the lymphoid tissues of *Pten*$^{+/R173C}$ mice, the
383 lymphoid phenotypes correlate with loss of nuclear PTEN as this phenotype was also seen in *Pten*$^{+/m3m4}$
384 mice (Jaini et al., 2020).
385
386 **Macrocephaly, increased neuronal complexity and white matter disturbances in *Pten*$^{+/R173C}$ mice**
387 PHTS patients, including the majority of patients with PTEN-R173 mutations (**Supplementary Table 1**),
388 commonly present with macrocephaly, DD and ASD. We therefore explored neurological and
389 behavioural phenotypes in *Pten*$^{+/R173C}$ mice.
390 We examined the brains and neurons from *Pten*$^{+/+}$, *Pten*$^{+/R173C}$ and *Pten*$^{+/-}$ mice and, where possible,
391 conditional knock-out mice that selectively lack PTEN expression in cortical pyramidal neurons
392 (referred to here as cKO) (Kessaris et al., 2006, Lesche et al., 2002). These cKO mice were further
393 crossed with *Pten*$^{+/R173C}$ mice to obtain conditional knock-in mice (referred to here as cKI) which
394 express PTEN-R173C in cortical pyramidal neurons without a copy of the PTEN-WT allele and are
395 overall hemizygous for the *Pten*^{R173C} allele (*Pten*$^{-/R173C}$). The observed phenotypes are summarized in

Table 2, which also shows a comparison to phenotypes published for *Pten*$^{m3m4/m3m4}$ mice. The latter model germline expression of non-naturally occurring PTEN mutations that leave PTEN PIP_3 phosphatase activity intact but lead to its nuclear exclusion, and whose neuronal phenotypes have been extensively characterised (Mester et al., 2011, Tilot et al., 2014, Jaini et al., 2020).

We first assessed the levels of PTEN protein and downstream pathways in protein lysates from cortical neurons. In the absence of a PTEN-WT allele, the level of PTEN protein in cKI was minimal and similar to that seen in protein extracts of cKO mice (**Fig. S13A-B**). However, the level of AKT P-S473 in cKI brains was significantly lower compared to the cKO mice (**Fig. S13A and C**). These observations mirror our data in MEFs (**Fig. S7**), indicating that PTEN-R173C is also highly active in the brain despite its low level of expression.

At 3 months of age, *Pten*$^{+/R173C}$ and *Pten*$^{+/-}$ mice of both sexes had enlarged brains with increased mass compared to *Pten*$^{+/+}$ littermates (**Fig. 4A-B, left panel**). Whole-body mass was also increased in both *Pten* mutant genotypes (**Fig. 4B, middle panel**), however, the brain was disproportionally enlarged (**Fig. 4B, left panel**), indicating a macrocephalic phenotype. Also, at 3- and 6-months of age, and independent of the genetic background, *Pten*$^{+/R173C}$ and *Pten*$^{+/-}$ mice showed a similar increase in brain mass (**Fig. S14**). Given the apparently normal PI3K/AKT regulatory capacity of PTEN-R173C, and the neurological phenotypes and macrocephaly previously observed in nuclear-excluded PTEN in heterozygous *Pten*$^{+/m3m4}$ and homozygous *Pten*$^{m3m4/m3m4}$ mice (Mester et al., 2011, Tilot et al., 2014), these observations allow us to postulate that the nuclear function of PTEN is key to the development of macrocephaly.

We next quantified several brain parameters to characterize the macrocephalic phenotype in more detail. *Pten*$^{+/R173C}$ mice had increased cortical thickness as measured at the level of the somatosensory barrel field (**Fig. 4C-D**). A significant increase was also observed in the thickness of the corpus callosum at four different Bregma levels (**Fig. 4E**) in both *Pten*$^{+/R173C}$ and *Pten*$^{+/-}$ mice. Consistent with macrocephaly, a lengthwise enlargement of the corpus callosum as well as an increase in the total area of this white matter tract at Bregma level were also observed (**Fig. 4F**). The increased thickness of the cortex was not caused by increased NEUN+ neuronal cell numbers or neuronal densities (**Fig. 4G**). In contrast, immunohistochemistry for OLIG2 revealed a small but significant increase in OLIG2-expressing oligodendrocyte lineage cell numbers in the cortex of *Pten*$^{+/R173C}$ mice (**Fig. 4H**). Interestingly, this increase was not seen in our *Pten*$^{+/-}$ mice and has not been reported in *Pten*$^{+/m3m4}$ mice but was observed in *Pten*$^{m3m4/m3m4}$ mice. Astrocyte overabundance and astrogliosis, as detected by GFAP immunostaining, were not observed (**Fig. 4H**). Interestingly, astrogliosis has been reported in *Pten*$^{m3m4/m3m4}$ mice, suggesting that the remaining wild type *Pten* allele protects the brain from this immunoinflammatory phenotype.

To gain further insight into the causes of the macrocephaly, we quantified neuronal and glial parameters *in vitro*. Morphologies of cortical pyramidal neurons *in vitro* were assessed following transfection with a GFP expression vector to allow visualisation of the cells (**Fig. 5A**). *Pten*$^{+/R173C}$ neurons had enlarged cell body size and increased process complexity compared to WT controls (**Fig. 5B,C**). While cKO neurons demonstrated a more severe phenotype, this phenotype was not observed in *Pten*$^{+/-}$ neurons and not reported in *Pten*$^{+/m3m4}$ mice but was observed in *Pten*$^{m3m4/m3m4}$ mice (**Fig. 5B,C**).

To determine whether glial and/or axonal defects contribute to the enlargement of the white matter, we examined the corpus callosum of *Pten*$^{+/+}$, *Pten*$^{+/R173C}$ and *Pten*$^{+/-}$ mice using transmission electron microscopy (**Fig. 5D**). We found a small increase in average axonal diameter in *Pten*$^{+/R173C}$ mice, with a reduction in the number of small diameter axons and a gain of larger diameter axons (**Fig. 5E**). This phenotype was not observed in *Pten*$^{+/-}$ mice. Quantification of the G-ratio in the corpus callosum showed an increase in average myelin thickness in both *Pten*$^{+/R173C}$ and *Pten*$^{+/-}$ mice (**Fig. 5F**). However, scatter plot analysis of the g-ratio as a function of axonal diameter did not show significant changes in either *Pten*$^{+/R173C}$ and *Pten*$^{+/-}$ mice compared to controls (**Fig. 5G**).

Altogether, our experiments show that the macrocephalic *Pten*$^{+/R173C}$ phenotype is caused by alterations in multiple parameters, including increases in neuronal cell body size, axonal thickness, axonal complexity and oligodendrocyte lineage cell numbers.

447 *Pten*$^{+/R173C}$ mice have a similar degree of macrocephaly as *Pten*$^{+/m3m4}$ heterozygous mice and have
448 multiple neuronal phenotypes overlapping with *Pten*$^{m3m4/m3m4}$ homozygous mice and *Pten*$^{+/-}$ mice
449 (**Table 2**). Importantly, the apparently intact or even increased PI3K/AKT regulatory capacity of PTEN-
450 R173C, and the phenotypic overlap with *Pten*^{m3m4} mice, suggests that the nuclear function of PTEN is
451 key to the development of macrocephaly and several neuronal phenotypes.
452 Defective dsDNA damage repair is increasingly being associated with macrocephaly and ASD with
453 studies showing increased dsDNA breaks in cells isolated from patients with these phenotypes (Wang
454 et al., 2020, Attia et al., 2020). To explore the possible involvement of impaired dsDNA damage repair
455 in neurons in the macrocephalic phenotype, we treated *Pten*$^{+/-}$ and *Pten*$^{+/R173C}$ mice with IR and
456 examined the levels of γH2AX in the brain 5 h post-IR treatment. While there was an increase in the
457 γH2AX levels in protein extracts from the brains of both *Pten*$^{+/-}$ and *Pten*$^{+/R173C}$ mice, compared to that
458 seen in littermate wild-type mice, the difference observed was not statistically significant (**Fig. S15**).
459 This might be due to the IR dosage and/or time of analysis, and warrants further investigation.
460
461 ***Pten*$^{+/R173C}$ mice display mild behavioural aberrations**
462 ASD is common in PHTS (Yehia et al., 2020). Behavioural abnormalities are found in mice with germline
463 expression of heterozygous loss-of-function of *Pten* (Clipperton-Allen and Page, 2014) or homozygous
464 expression of the nuclear-excluded *Pten*^{m3m4} (Tilot et al., 2014). To examine such type of aberrations
465 in *Pten*$^{+/R173C}$ mice, we used a range of tests associated with ASD-like mouse behaviours.
466 In Crawley's sociability test, *Pten*$^{+/R173C}$ mice were indistinguishable from *Pten*$^{+/+}$ littermate controls,
467 indicating normal social interactions (**Fig. S16A-D**). In the open field test, male mice were not
468 significantly different from their *Pten*$^{+/+}$ littermates with regards to distance travelled in the open field
469 arena and time spent moving during the test (**Fig. S17B,C**). However, female *Pten*$^{+/R173C}$ mice travelled
470 less and spent less time moving than WT controls (**Fig. S17F,G**), suggesting decreased exploratory
471 behaviour and/or decreased locomotion. This was not caused by increased anxiety since female (and
472 male) mice spent equal length of time exploring the different compartments of the open field test as
473 their WT controls (**Fig. S17D,H**), with defecation during the test being comparable between the two
474 groups (**Fig. S17E,I**). Reduced exploratory locomotion in females was also observed in a hole board
475 test (**Fig. S18A**). Changes in repetitive behaviours, as assayed in a marble burying test were absent in
476 both males and females (**Fig. S18B**).
477
478 **DISCUSSION**
479 Since the discovery of PTEN as a tumour suppressor in somatic cancer, multiple genetic mouse models
480 targeting *Pten* have been generated, highlighting the importance of PIP_3 phosphatase activity of PTEN
481 in tumour suppression, embryonic development, cellular homeostasis, neuronal development and the
482 development of autism spectrum traits (Lee and Pandolfi, 2020).
483 PTEN mouse models have also improved our understanding of PHTS, a rare genetic condition
484 caused due to heterozygous germline *PTEN* mutations. These include *Pten*$^{+/-}$ mice which represent the
485 heterozygous genetic constellation of *PTEN* in PHTS and on a mixed C57BL6xSv129 background
486 develop multiple phenotypes overlapping with the clinical presentation of PHTS, including brain and
487 lymphoid overgrowth and the development of specific cancers (Tibarewal et al., 2022). While the PIP_3
488 phosphatase activity of PTEN has been the focus of research over the last three decades, there is an
489 increasing body of evidence for other PTEN functions in disease pathogenesis, in particular its nuclear
490 function (Langdon, 2023). Recently, the *Pten*^{m3m4} mouse model with germline expression of nuclear-
491 excluded, engineered non-naturally-occurring *Pten* mutations, has indicated a role for nuclear PTEN
492 defects in driving neuronal and immune phenotypes in PHTS (Tilot et al., 2014, Jaini et al., 2020).
493 In this study, we developed a new mouse model featuring the pathogenic PTEN-R173C variant
494 commonly found in PHTS and somatic cancer. We report that this PTEN variant retains its ability to
495 regulate PI3K/AKT signalling but is impaired in dsDNA damage repair through HR, likely due to nuclear
496 exclusion. Contrary to previous reports (Han et al., 2000, Smith and Briggs, 2016, Post et al., 2020), we
497 found that PTEN-R173 mutant proteins (R173C and R173H) were catalytically more active PIP_3 lipid

phosphatases than PTEN-WT, both in cells and tissues. However, these mutants displayed reduced protein stability, possibly resulting from a more open protein configuration that is more susceptible to ubiquitination-mediated degradation. Upon heterozygous germline expression in *Pten*$^{+/R173C}$ mice, this biochemical feature results in PTEN protein expression levels comparable to those in *Pten*$^{+/-}$ mice but an overall lipid phosphatase activity similar to wild-type mice, as demonstrated by effective downregulation of insulin-stimulated PI3K/AKT signalling.

Pten$^{+/-}$ mice with heterozygous PTEN loss are predisposed to a range of tumours similar to those observed in PHTS patients (Tibarewal et al., 2022). To assess the importance of nuclear functions of PTEN in tumourigenesis, we aged *Pten*$^{+/R173C}$ mice and found only a modest predisposition to solid tumour development compared to *Pten*$^{+/-}$ mice. This is reminiscent of mouse models of genes involved in dsDNA damage repair via HR such as *Brca*, *Rad51* and *Palb2* (Matos-Rodrigues et al., 2021, Tsuzuki et al., 1996, Roy et al., 2011, Rantakari et al., 2010, Yan et al., 2004, Hakem et al., 1996). Indeed, while homozygous inactivation of these genes frequently leads to embryonic lethality, as also observed in *Pten*$^{R173C/R173C}$ mice, their heterozygous inactivation only leads to a very low to absent tumour burden, most likely because the lifespan of mice is insufficiently long to accumulate the additional mutations required for tumourigenesis (Drost and Jonkers, 2009). That additional genetic defects may be required to allow phenotypic output of PTEN-R173 defects is indicated by the observation that somatic cancers with PTEN-R173 mutation have a range of co-occurring mutations, including but not limited to oncogenic mutation in *PIK3CA* or loss of second allele of *PTEN* (**Fig. 3D**). Also in mouse models, combination of *Pten* mutations with other oncogenic drivers such as mutant *Pik3ca* and *ErbB2* have accelerated development of mammary tumours (Kato et al., 2020, Yip et al., 2020). Combining the *Pten-R173C* mutation in mouse models carrying additional cancer drivers (such as *PIK3CA* mutation) or defects in DNA repair genes (such as *Brca* or *Rad51*) could provide evidence for this speculation, but such experiments are outside the scope of the current study.

Our data further show that, in a germline configuration, deficient nuclear localisation of PTEN, and consequently its nuclear function, correlates with brain and lymphoid overgrowth. While our study does not establish a direct correlation between these overgrowth phenotypes in our mice and dsDNA damage repair, it is possible that such a link exists. Indeed, one study reported increased IR-induced DNA strand breaks in lymphocytes from autistic children compared to non-autistic controls supporting such a functional link (Attia et al., 2020). On the other hand, lymphoid cells isolated from PHTS patients with PTEN-R173C mutation, who all present with ASD, did not exhibit increased DNA damage following IR treatment compared to wild-type controls (Wei et al., 2024), suggesting that nuclear functions of PTEN other than dsDNA repair may underlie the observed lymphoid overgrowth and macrocephaly in *Pten*$^{+/R173C}$ mice. This is further supported by the absence of lymphoid overgrowth and macrocephaly in patients and mouse models with germline mutations in other genes regulating dsDNA damage repair by HR, such as the *Brca*, *Rad51* and *PalB2* genes.

We find that the macrocephalic *Pten*$^{+/R173C}$ phenotype correlates with alterations in multiple parameters, including increases in neuronal cell body size, axonal thickness, axonal complexity and oligodendrocyte lineage cell numbers. While this brain overgrowth phenotype in *Pten*$^{+/R173C}$ mice is very clear, its impact on animal behaviour is less prominent. It has to be said that while mice with heterozygous germline expression of PTEN accurately reflect the genetic makeup of patients with PHTS, the behavioural abnormalities observed in heterozygous mutant mice are often subtle and highly variable (Clipperton-Allen and Page, 2014). This necessitates large mouse numbers to achieve quantifiable significant differences between genotypes. Consequently, the field of behavioural analysis has mostly relied on the use homozygous mouse models. This approach is particularly true for PHTS, with numerous studies conducted on homozygous brain-specific PTEN knockout models (Kwon et al., 2006, Zhou et al., 2009) and homozygous *Pten*^{m3m4} models (Tilot et al., 2014). Similar homozygous models are also utilized in behavioural research on other rare diseases such as Tuberous Sclerosis (Yuan et al., 2012, Bateup et al., 2013). Although these models do not share the exact genetic composition of patients, they serve as platforms for behavioural and neurological studies and testing therapeutics.

549 Our study suggests that the status of nuclear function of PTEN alongside its PIP_3 phosphatase
550 activity, allows refinement of genotype/phenotype analysis in PHTS. Based on our findings and
551 assessment of patient phenotypes (**Table 1** and **Supplementary Tables 1 and 2**), our data indicate that
552 individuals carrying *PTEN* variants such as $PTEN^{R173C}$ that retain their PIP_3 phosphatase function but are
553 nuclear-excluded tend to follow a characteristic progression of known PHTS disease phenotypes: early-
554 signs such as neurological abnormalities – including macrocephaly and global developmental delay -
555 alongside cutaneous features which together lead to a PHTS diagnosis during childhood. As they enter
556 early adulthood, they may be prone to developing vascular abnormalities and benign tumours in the
557 thyroid and GI tract, with an increased likelihood of developing malignant cancers later in life.
558 Our study also highlights the possibility of new therapeutic treatments for cancer in PHTS patients.
559 A previous study has shown that glioma cells expressing PTEN-Y204F, a mutation that leads to lack of
560 PTEN nuclear localisation and functions such as dsDNA damage repair are more sensitive to radiation
561 therapy (Ma et al., 2019). It is therefore tempting to speculate that radiation therapy and dsDNA
562 damage repair antagonist drugs, such as *PARP* inhibitors, might be additional therapeutic options
563 beyond PI3K pathway inhibitors for cancer in PHTS patients with R173 mutant-like PTEN variants.
564

565 **Methods**

566 **Plasmids**. DNA constructs are detailed in **Supplementary Table 8**. Point mutations were introduced in
567 PTEN WT cDNA in different vectors using primers listed in **Supplementary Table 9** and KOD hot start
568 DNA polymerase (Sigma-Aldrich) using the manufacturer's instructions.
569 **Mice.** All mice were maintained at University College London in accordance with the UK Animals
570 (Scientific Procedures) Act 1986 and following UK Home Office guidance. All procedures were
571 authorized by a UK Home Office Project Licence subject to local ethical review. *Pten*$^{+/-}$ mice
572 (Podsypanina et al., 1999), *Pten*$^{flox/flox}$ mice (Lesche et al., 2002), *CAG CreER*^{T2} mice (Schonhuber et al.,
573 2014) and *Emx1-Cre* mice (Kessaris et al., 2006) have been described elsewhere. *Pten*$^{+/R173C}$ mice were
574 generated by Taconic Biosciences using a CRISPR/Cas9 approach. gRNA was designed to contain the
575 R173C mutation (c.517C>T) and a silent mutation containing the *Eco*NI restriction site upstream of the
576 R173 site (to allow discrimination of wild-type and knock-in allele following PCR). **Fig. S6** shows the
577 gRNA sequence and the targeting strategy. gRNA was microinjected into C57BL/6J mouse zygotes
578 along with recombinant Cas9. The zygotes were then transferred to pseudo-pregnant mothers. The
579 litters born (founder animals) were sequenced to check for the incorporation of the R173C mutation
580 and percentage of mosaicism. They were then used to as a breeder to generate F1 animals. F1 males
581 positive for the R173C mutation and negative for any off-target mutations were used to generate
582 further animals by IVF using C57BL/6J females. All mouse lines were maintained on a C57BL/6J
583 background. Sv129 mice were purchased from Charles River or Envigo. *Pten*$^{+/-}$ and *Pten*$^{+/R173C}$ mice
584 were crossed with Sv129 mice to obtain mixed background F1 mice that were used for some
585 experiments as described. For neuronal studies, conditional knock-out mice that selectively lack PTEN
586 expression in cortical pyramidal neurons *were generated by crossing Pten*$^{flox/flox}$ mice with *Emx1-Cre*
587 mice to give *Emx1-Cre*;*Pten*$^{fl/fl}$; referred to here as cKO. The cKO mice were crossed with *Pten*$^{+/R173C}$
588 mice to obtain *Emx1-Cre*;*Pten*$^{fl/R173C}$,referred to here as cKI, which express one only copy of *Pten*-R173C
589 in the cortical pyramidal neurons.
590 For genotyping, mouse tissue samples (from ear biopsy or from the embryonic yolk sac) were lysed in
591 25 mM NaOH/0.2 mM disodium EDTA for 1 h at 95°C. The samples were neutralized by adding an
592 equal volume of a buffer containing 40 mM Tris-HCl, pH 4.5. Two µl of the DNA extract was used for
593 PCR using and Titanium polymerase PCR kit (Takara) and primers listed in **Supplementary Table 10**.
594 For genotyping of *Pten*$^{+/R173C}$ mice, an additional restriction digestion step was performed on the PCR
595 products using *Eco*NI (New England Biolabs).
596 **Mouse survival studies.** For sample size calculations for long term survival study, we use ClinCalc
597 (www.clincalc.com). The mean survival age of *Pten*$^{+/-}$ on a mixed C57BL6J x Sv129 background has been
598 reported to be 12±1.8 months (Alimonti et al., 2010). The sample size required for *Pten*$^{+/R173C}$ mice
599 needed to see a 15% improvement in mean survival age compared to *Pten*$^{+/-}$ mice was calculated as
600 16 (probability of Type-I error was set to 0.05 and Power was set to 80%). We used at least 16 mice
601 for each genotype and each sex. At least 10 Littermate wild type mice were used for both *Pten*$^{+/-}$ and
602 *Pten*$^{+/R173C}$ mice. For survival analysis, mice were weighed twice a week. They were monitored and
603 euthanized upon showing a more than 20% reduction in body weight, any signs of ill health such as
604 hunched appearance, laboured breathing, sluggish behaviour, or palpable masses with a total surface
605 area of 1.4 cm^2 surface area. Animals showing no clinical signs were euthanized at the end of the study
606 (600 days for females and 730 days for males).
607 **Cell lines.** U-87 MG (U87), HEK-293T and Phoenix cells were purchased from ATCC, Lenti-X™ 293T cells
608 were purchased from Clontech. Human PTEN knockout HeLa cell line and control HeLa cells was
609 obtained from Abcam (ab255419 and ab255928); PTEN knockout was validated using western blotting
610 (**Fig. S4C**). All cell lines were maintained in DMEM (Sigma-Aldrich), supplemented with 10% Filtered
611 Bovine Serum (FBS) (Pan-Biotech) and Pen-Strep (Sigma-Aldrich) using standard cell culture methods.
612 **Preparation of MEFs.** For preparation of E13.5 MEFs, timed matings were set up between *Pten*$^{+/-}$ mice
613 and *Pten*$^{+/R173C}$ mice, *Pten*$^{flox/+}$*CreER*^{T2} and *Pten*$^{+/-}$ or *Pten*$^{+/R173C}$ mice. Pregnant females were euthanized
614 on day 13.5 and embryos harvested from the uterus. Following removal of the head and visceral
615 organs, the rest of the embryo was minced in 2x Trypsin/EDTA using a sterile scalpel and incubated at

616 37°C for 40 min. The cell suspension was plated on 10 cm dishes in DMEM (Sigma-Aldrich) medium
617 supplemented with 10% FBS (Pan-Biotech) and Pen-Strep (Sigma-Aldrich), and cells maintained using
618 standard cell culture procedures. For preparation of E9.5 MEFs, timed intercrosses were set up
619 between *Pten*$^{+/R173C}$ mice. Pregnant females were euthanized on day 9.5, embryos removed from the
620 uterus and gently dissociated by pipetting up and down using a p1000 pipette and 2 ml of media
621 containing DMEM (Sigma-Aldrich), supplemented with 10% FBS (Pan-Biotech) and Pen-Strep (Sigma-
622 Aldrich). The cell suspension was plated in 48-well plates and cells maintained using standard cell
623 culture procedures. To induce Cre-mediated recombination of the floxed *Pten* allele in *Pten*$^{flox/+}$*CreER*^{T2}
624 MEFs, 4-hydroxy tamoxifen (Sigma Aldrich) was added to the cells at a final concentration of 1 µM and
625 refreshed every 24 h for 3 days.
626 **Primary neuron culture.** Primary cortico-hippocampal cultures were prepared from P1 or P2 pups
627 after genotyping. Cortex and hippocampus were dissected, digested with Trypsin, dissociated using
628 glass pipettes and 40,000 cells were plated per 12 mm coverslip. Neurons were cultured in serum-free
629 medium (neurobasal, NBA) medium supplemented with B27 supplement, L-glutamine,
630 penicillin/streptomycin and 10 mM HEPES pH 7.4. Cells were cultured at 5% CO_2 at 37°C with
631 replacement of half of the medium every 2-3 days. Cells were transfected on DIV6 with a GFP
632 expression vector using Lipofectamine 3000 according to the manufacturer's instructions. On DIV
633 12/13 cells were fixed with 4% PFA/4% sucrose in PBS for 10 min at room temperature (RT) and washed
634 3x in PBS. Cells were blocked and permeabilized in immunofluorescence (IF) buffer (PBS supplemented
635 with 0.3% Triton X and 3% BSA) for 20 min and incubated with primary antibodies to NeuN (Millipore
636 MAB377 and GFP, Abcam 1:1000) for 2 h at RT in IF buffer in a humidity chamber. After 3 washes with
637 PBS, cells were incubated with cross-absorbed Alexa Fluor labelled secondary antibodies (Invitrogen)
638 in IF buffer for 1 h at RT in a humidity chamber in the dark, washed 3x with PBS and mounted with
639 Immunomount. Neurons were imaged using a LSM 880 microscope (Leica) acquiring Z-stacks at 40 x
640 magnification. Dendritic complexity was determined using the Sholl macro in FIJI. Interceptions were
641 analysed in 10 µm radii within a 200 µm distance from the centre of the soma. To measure cell body
642 size in FIJI, stacks were processed to z-projections, ROIS were drawn manually around the cell bodies
643 and the ROI area was measured in FIJI.
644 **PTEN activity assays.** For purification of bacterially-expressed GST-tagged PTEN proteins, pGEX6P1
645 vectors with cDNA for WT or mutant PTEN were introduced in *E. coli* and recombinant PTEN was
646 purified by glutathione-affinity chromatography followed by cleavage of the GST tag as described
647 (Davidson et al., 2010). PIP_3 assays using purified recombinant PTEN were performed with diC8 PIP_3
648 (Cell Signals Inc) and malachite green phosphate assay kit (Sigma Aldrich) and have been described
649 elsewhere (Maehama and Dixon, 1998). Purification of recombinant PTEN protein from insect cells
650 was as described in Ref.(Masson et al., 2016b).
651 **Lentiviruses and retroviruses**. Lentiviruses for PTEN and PIP_3 biosensor were generated by co-
652 transfecting Lenti-X™ 293T cells or HEK-293T cells with plasmids expressing the cDNA of interest along
653 with packaging vectors using TransIT-LT1 following the manufacturer's instructions. For preparation
654 of retroviruses, Phoenix cells were transfected with p53 shRNA expressing vector (Dickins et al., 2005)
655 using TransIT-LT1 following the manufacturer's protocol. 24 h post transfection, sodium butyrate was
656 added to the cells to a final concentration of 12.5 mM for 6 h, followed by washing the cells with warm
657 PBS and addition of fresh media. The supernatant containing lentiviral particles was collected after 20
658 h, passed through a 0.45 µm filter and stored at -80°C. Target-cells for transductions were plated at
659 40-50% confluency. Once the cells had attached, lentiviral/retroviral particles were added to the cells
660 along with polybrene (Sigma-Aldrich) at 20 µg/µl. The media was changed 24 h post transduction.
661 **Immunoblotting analysis**. Protein extracts from cell cultures were prepared by scraping cells into lysis
662 buffer containing 25 mM Tris-HCl pH 7.4, 150 mM NaCl, 1% Triton X-100, 10% glycerol, 1 mM EGTA, 1
663 mM EDTA, 5 mM sodium pyrophosphate, 10 mM β-glycerophosphate, 50 mM sodium fluoride, 1 mM
664 sodium orthovanadate, 1 mM DTT and Protease inhibitor cocktail (Millipore). Mouse tissues harvested
665 from mice upon euthanasia were homogenize using Lysing Matrix M tubes (MP Biomedicals) in double
666 the volume (v/w) of lysis buffer (25 mM Tris-HCl pH 7.4, 150 mM NaCl, 1% Triton X-100, 0.1% SDS, 10%

667 glycerol, 1 mM EGTA, 1 mM EDTA, 10 mM sodium pyrophosphate, 20 mM β-glycerophosphate, 100
668 mM sodium fluoride, 2 mM sodium orthovanadate, 1 mM DTT and protease inhibitors) on a FastPrep
669 24 homogeniser (MP Biomedicals) at 4 m/sec for 20 sec. Cell or tissue lysates were pre-cleared by
670 centrifugation at 20,000xg for 10 min and protein extracts analysed by immunoblotting. 293T cells
671 expressing Rluc-PTEN-YFP constructs were lysed in buffer containing 50 mM HEPES (pH 7.4), 250 mM
672 NaCl, 2mM EDTA, 0.5% NP-40, 10% glycerol supplemented with protease and phosphatase inhibitors
673 (Roche) and protein A/G PLUS-Agarose (30µl/IP) and GFP antibody (Roche, Cat #11814460001, Mouse,
674 Dilution 1:200) was used to immunoprecipitate YFP-tagged PTEN protein which was used for
675 immunoblotting as described below. Protein gel electrophoresis was conducted with 10 µg of total
676 soluble protein per lane on NuPage Bis-Tris 4-12% gradient polyacrylamide gels (Thermofisher
677 Scientific) following the manufacturer's protocols. Proteins were transferred onto PVDF membrane
678 (Millipore) and membranes blocked in 5% milk powder/TBST for 1 h at RT. Blocked membranes were
679 incubated overnight with primary antibodies (**Supplementary Table 11**). Antibody complexes were
680 detected by 1 h incubation at RT with HRP-conjugated secondary antibodies (GE healthcare). Blots
681 were developed with Immobilon Forte Western HRP substrate (Millipore) and chemiluminescence
682 imaged using an ImageQuant LAS4000 imaging system (GE healthcare).
683 **qRT-PCR assays.** Total RNA was extracted from U87cells non-transduced or transduced with
684 lentiviruses for PTEN-WT, PTEN-C124S, PTEN-R173C or PTEN-R173H, using RNAEasy kit (Qiagen)
685 following the manufacturer's instructions. 1 µg of RNA was converted to cDNA using iScript RT kit
686 (BioRad). 50 ng of cDNA was used for QRT-PCR reactions using primers in **Supplementary Table 12**.
687 The reactions were run on a QuantStudio™ 5 Real-Time PCR machine (Applied Biosystems). dCT was
688 calculated by deducting the CT for GAPDH from CT of PTEN. ddCT was calculated by deducting the dCT
689 of untransduced cells from the dCT of the sample of interest.
690 **Cycloheximide chase studies.** U87 cells were transduced with lentiviruses for PTEN-WT, PTEN-C124S,
691 PTEN-R173C or PTEN-D252G. 48 h post transduction, cells were treated with 200 µg/ml cycloheximide,
692 lysed at different time points and protein extracts analysed for PTEN expression by immunoblotting.
693 **BRET assays.** BRET assays using the Rluc-PTEN-YFP biosensor were performed as described in Refs
694 (Misticone et al., 2016, Lima-Fernandes et al., 2014). Briefly, 24 h post-transfection, cells were
695 detached from 12-well plates, using trypsin-EDTA, and resuspended in 1 ml of complete media. The
696 cells were subsequently distributed into poly-L-ornithine-coated (30 µg/ml) white 96-well optiplates
697 (Perkin Elmer). The next day media was replaced with Opti-MEM (Gibco) and Coelenterazine substrate
698 (Interchim) was added to a final concentration of 5 µM and incubated for 3 min at 25°C. BRET readings
699 were then collected using a Multilabel Reader Mithras2 LB 943 (Berthold Technologies). Sequential
700 integration of light output was measured for 1 sec using two filter settings (480+10nm for YFP and
701 540+20nm for Rluc). The BRET signal represents the ratio of the light emitted by YFP and the light
702 emitted by Rluc (YFP/Rluc). The ratio values were corrected by subtracting background BRET signals
703 obtained with Rluc-PTEN. MilliBRET (mBRET) values were calculated by multiplying these ratios by
704 1,000. Data are represented as specific mBRET values or ΔmBRET when compared to the signal
705 obtained with WT PTEN set to 0.
706 **MTS assays.** U87 cells were transduced with lentiviruses for GFP, PTEN-WT, PTEN-C124S, PTEN-R173C
707 or PTEN-R173H. 48 h post transduction, 5000 cells/well were plated in 96-well plates. A different plate
708 was prepared for each day. 20 µl of MTS assay reagent (Abcam) was added to the cells, incubated at
709 37°C for 1 h, followed by measurement of absorbance at 490 nm using a plate reader.
710 **PIP_3 biosensor analysis and PTEN localization using fluorescence microscopy.** For plasma membrane
711 PIP_3 quantification, U87-MG cells were transduced with lentiviral particles expressing the PIP_3
712 biosensor on its own or with lentiviral particles for PTEN-WT or PTEN-R173C, were pretreated ± GDC-
713 0941 (1 µM) for 1 h and stimulated ± insulin (100 nM) for 2 min. For PTEN localization studies, MEFs
714 were treated ± GDC-0941 (1 µM) 1 h prior to fixation. For both plasma membrane PIP_3 quantification
715 and localization of untagged or endogenous PTEN, cells were fixed with 4% PFA for 20 min, washed in
716 PBS, permeabilized with 0.1% Triton X-100 in PBS for 90 sec, washed 3 times with PBS and blocked
717 with PBS containing 1 or 3% (w/v) BSA for 30 min. Primary antibodies to PTEN were diluted in 1 or 3%

718 BSA block solution and incubated for 1 h at RT. Following 3 washes with PBS, secondary antibodies and
719 Phalloidin were diluted in 1 or 3% BSA block solution and incubated for 45 min at RT. Cells were then
720 washed 3 times and mounted using ProLong Gold antifade reagent containing DAPI (P36935, Life
721 Technologies). To examine GFP-PTEN localization during different stages of the cell cycle, Lenti-X™
722 293T cells were transfected with DNA for PTEN-WT-GFP or PTEN-R173C-GFP. 18 and 36 h post
723 transfection, culture medium was changed to fresh media containing 2 mM thymidine (Sigma). 18 h
724 post the second media change, the cells were released from double thymidine block by changing into
725 fresh, complete media. Cells were fixed with 4% PFA for 15 min, washed in 3 times in PBS and
726 permeabilized with 0.1% Triton X-100 in PBS for 5 min. Cells were then washed 3 times with PBS and
727 once with water before mounting using ProLong Gold antifade reagent containing DAPI. Confocal
728 microscopy was performed using a Zeiss LSM 880 microscope with AiryScan and a 63x PL APO objective
729 and Zen Black acquisition software or Zeiss LSM900 microscope and a 63x or 40x PL APO objective and
730 Zen Black acquisition software. Image processing was performed using Image J software (National
731 Institutes of Health, Rockville, MD, United States) and was limited to alterations of brightness,
732 subjected to the entire image. Quantification of plasma membrane PIP_3 intensity was performed using
733 Image J as described previously with minor modifications (Ooms et al., 2015). The average
734 fluorescence intensity was measured within a box of defined size (20 x 10 pixels) at three random
735 regions of the plasma membrane and three random regions of the cytosol (box size 20 x 20 pixels).
736 The plasma membrane and cytosol fluorescence intensity measurement were each averaged and the
737 ratio of plasma membrane to cytosolic fluorescence intensity determined. The PTEN nuclear to
738 cytoplasmic ratio was measured using Image J. First, the nuclear PTEN fluorescence intensity was
739 measured, followed by the cytoplasmic PTEN fluorescence intensity. The ratio of nuclear to
740 cytoplasmic PTEN fluorescence intensity was then calculated.
741 **Insulin tolerance test (ITT).** 3-month-old male *Pten*$^{+/-}$ and *Pten*$^{+/R173C}$ mice and their WT littermates
742 were starved for 6 h. The tip of the tail was punctured using a 26G needle and time-0 blood glucose
743 levels were recorded using a standard glucometer. The mice were given an IP injection of insulin to a
744 final concentration of 0.75 U/kg. Blood glucose readings were recorded at 15 min, 30 min, 45 min, 60
745 min, 90 min and 120 min post injection.
746 **Irradiation of mice:** 8-12-week-old mice were subjected to whole body irradiation of 7 Gy dose using
747 the Small Animal Radiation Therapy Platform (SARRP). 5 h post irradiation, the mice were euthanised
748 with a lethal injection of pentobarbital. Tissues of interest were harvested and snap frozen in liquid
749 nitrogen for biochemical analysis.
750 **Flow cytometry.** Mouse spleens and lymph nodes were mashed with a syringe plunger in RPMI
751 containing 10% FBS and filtered through a 70 µm filter. Cell suspensions from spleen were treated with
752 RBC lysis buffer (Biolegend). The cell suspensions were washed with PBS and stained with Fixable
753 Viability Dye eFluor™ 780 (ThermoFisher scientific) in PBS for 40 min followed by a few PBS washes.
754 For staining of surface antigens, antibodies were diluted in FACS staining buffer at 1:100 and added to
755 the cells for 30 min followed by two washes with FACS buffer. Details on antibodies and reagents used
756 is shown in **Supplementary Table 11**. The stained cells were analysed on BD FACSymphony™ analyser.
757 **Tissue processing for histological analysis and immunohistochemical analysis.** Mouse tissues were
758 fixed in 10% neutral buffered formalin for 24 h, followed by processing and embedding into paraffin
759 blocks. The tissues were orientated with the biggest surface down, to obtain complete sections. 3 µm
760 serial sections were cut and stained for Haematoxylin and Eosin, followed by immunohistochemistry
761 staining on the Leica BOND Rxm. Tissue sections for immunohistochemistry were incubated for 40 min
762 at 100°C in BOND epitope retrieval solution 2 (Leica, Germany), followed by blocking and staining using
763 the BOND polymer refine detection kit (Leica, DS9800), primary antibody (**Supplementary Table 11**)
764 and DAB enhancer (Leica, Germany).
765 **Histopathological analysis.** Non-neoplastic lesions, e.g. splenic extramedullary haematopoiesis and
766 lymph node hyperplasia, were graded using a standard semi-quantitative grading scheme from 0 to 5,
767 where 0 = lesion not present and 5 = the maximum lesion size/extent (Scudamore, 2014). In general,
768 where present, the presence of other proliferative lesions including hyperplasia and neoplasia was

769 recorded for each individual organ, allowing the overall incidence to be established for each lesion in
770 each group. Prostatic intraepithelial neoplasia (PIN) was graded as low or high grade according to the
771 consensus suggested by Ittmann *et al.* (Ittmann et al., 2013). Low-grade PIN lesions are focal, with one
772 to two layers of cells and mild nuclear atypia. High-grade lesions tend to be more extensive, filling the
773 prostatic lumen but without stromal invasion; have two or more cell layers often forming papillary or
774 cribriform patterns; increased nuclear atypia and mitoses.
775 **Perfusion and preparation of brain sections for DAB immunostaining and immunofluorescence.** Mice
776 were perfused with saline (0.9 % NaCl) followed by 4% PFA (w/v) in PBS through the left ventricle of
777 the heart. Brains were removed and post-fixed overnight at 4°C in 4% PFA, cryoprotected in 20%
778 sucrose in PBS for 24 h at 4°C and embedded in Tissue-Tek OCT compound (Sakura) in isopentane
779 cooled on dry ice. Frozen brains were stored at -80°C until use. Brains were processed on a Cryostat
780 (30 µm thickness) and sections were collected in PBS for immunohistochemistry. For DAB
781 immunostaining, floating sections were incubated with 0.3 % H_2O_2 in PBS for 30 min while shaking at
782 RT, and then blocked using blocking buffer (10% FBS in PBS supplemented with 0.1% Triton X-100) for
783 1 h at RT. After blocking, sections were incubated overnight at 4°C with primary antibodies diluted in
784 blocking buffer. Primary antibodies were detected with biotinylated secondary antibodies (Donkey
785 Anti-Mouse IgG Biotinylated Antibody, R&D systems) diluted 1:300 in blocking buffer for 1 h at RT. The
786 signal was amplified using the Vectastain ABC Kit HRP kit (Vector, PK-6100), according to the
787 manufacturer's instructions and developed using a DAB Peroxidase (HRP) Substrate Kit (Vector, SK-
788 4100) until the desired staining intensity was reached. Floating sections were mounted on Superfrost
789 plus slides in 0.2 % pork skin gelatine dissolved in 50 mM Tris-HCl pH 7.4, dried at RT overnight and
790 dehydrated in ethanol and xylene before mounting with DPX mounting medium (Merck). Images were
791 acquired using 20x magnification on a ZEISS Axio Scan.Z1 microscope and processed using ZEISS ZEN
792 lite software. For immunofluorescence, sectioned brains were blocked for 1 h before primary
793 antibodies were applied overnight. AlexaFluor 488 secondary antibody was used to detect OLIG2
794 (1:1000; Invitrogen, Carlsbad, CA) for 60 min at room temperature together with Hoechst 33258
795 (1:1000; Sigma) to detect cell nuclei. All secondary antibodies were diluted in block solution. Floating
796 sections were transferred onto Superfrost plus slides (BDH Laboratory Supplies) and air dried before
797 being coverslipped with Dako fluorescent mounting medium.
798 **Analysis of corpus callosum and cortex thickness and cell counting.** Matched sections at specified
799 Bregma levels were measured using the Zeiss Blue software measurement length tool. Counting boxes
800 were positioned onto matched slices in the barrel field of the primary somatosensory cortex
801 perpendicular to the corpus callosum. In each box, cells were counted from the border of the corpus
802 callosum to the pial surface. The length of the box was adjusted to fit the cortical thickness while the
803 width was not changed. All cells positive for NeuN within the box were counted and cell numbers
804 displayed as crude numbers in the box as well as density considering the area of the boxes analysed.
805 Four animals per genotype were used.
806 **Electron microscopy (EM).** EM was performed as described in Ref.(Kougioumtzidou et al., 2017).
807 Briefly, mice were prepared for EM by PBS perfusion followed by 2.5% (v/v) glutaraldehyde and 2%
808 (w/v) paraformaldehyde in 0.1 M sodium cacodylate buffer (pH 7.6). Brains were removed and kept
809 at 4°C for 48 h in the same fixative, before being washed with 0.1 M cacodylate buffer, rinsed briefly
810 with 0.1 M phosphate buffer and shipped to Japan at ambient temperature. Sagitally-sectioned brains
811 were processed for EM. After immersion in a 1% (w/v) osmium tetroxide solution for 2 h at 4°C, the
812 specimens were dehydrated through a graded alcohol series and embedded in Epon 812 (TAAB
813 Laboratories, UK). The required area was trimmed, and ultrathin sections were cut, collected on a
814 platinum-coated glass slide, stained with uranyl acetate and lead citrate and imaged in a scanning
815 electron microscope equipped with a back-scattered electron beam detector (Hitachi SU8010) at 1.5
816 kV accelerating voltage. EM images of sagittal sections of corpus callosum were taken at 15000x
817 magnification. To estimate g-ratios, the circumference of the axon and the external circumference of
818 the myelin sheath were measured using ImageJ, avoiding paranodal areas. The diameters of axon and

myelin sheath were calculated from these circumferential measurements, assuming a circular profile, and the g-ratio was calculated.

Behavioural analysis. Behaviour testing was carried out as previously described (Magno et al., 2021). 12-week-old mice on mixed C57BL/6 x Sv129 background were used in this study. All animals were kept on a 12 h light-dark cycle with food and water accessible ad libitum. The indicated numbers of WT mice and their *Pten*$^{+/R173C}$ littermates were tested in the open field test, three chambers test, hole board and marble burying. Mice tested in behavioural experiments were habituated to handling and the experimenter for 9 days before the start of behavioural experiments to reduce stress and habituated mice were generally handled by cupping. Mice were analysed in three cohorts and male and female mice were tested on separate days. During experiments white noise was played at around 50 Db to mask external noises and all experiments were video recorded. Before every experiment, mice were brought into the behavioural room 30 min before the first experiment for habituation and animals that had finished a test were transferred into a new cage in order not to influence the behaviour of the remaining experimental animals. Directly before the first experimental animal was tested and after every mouse the set up (open field, sociability chamber, hole board) was cleaned thoroughly with water and 70% ethanol in a consistent manner for every animal. Open field: the experimental animal was placed in an open field box measuring 30 cm x 30 cm. The walls were white and 40 cm high so that the animal could not get any visual clues. The mouse was allowed to roam freely for 30 min to explore the arena without any prior habituation. Distance, time spent in different areas and the time moving were analysed using Ethovision software while faecal boli were counted manually. Sociability: The experimental animal was placed into the central compartment of Crawley's chamber for 5 min with closed doors for habituation. After 5 min empty cages were placed into the middle of the left and right compartments and a stranger mouse was gently put into one of the cages (counterbalance left and right sides). The stranger mouse matched the subject mouse with regards to the breeding background, age and gender and had no contact with the subject mouse ever before. Both doors were opened at the same time and the experimental mouse was allowed to explore the area for 10 min. A stopwatch was used to determine the time the subject mouse spent closely interacting with either cage (direct contact/sniffing/cage climbing). The time spent with the empty cage versus the first stranger was measured, referred to as sociability. Calculation of discrimination indices: (time spent with mouse – time spent with empty cage)/(sum of the time spent with both). Hole board: since the experimental animals were familiar with the open field arena from the open field experiment, they were only briefly re-exposed to the empty arena for 10 min on day 1 of the hole board test. On the next day a hole board with 16 holes evenly spaced was placed into the arena, the subject mouse was put into the middle of the field and was recorded for 15 min. A manual cell counter was used to determine the total number of head dips into the holes. Marble burying: a cage was filled with 5cm of bedding that was tamped down lightly to produce an even surface. 12 glass marbles were distributed evenly spaced out in the cage and the animal was allowed to roam freely for 15 min. Marbles that were buried to 2/3 of their depth with bedding were counted.

Statistical analysis: GraphPad Prism (San Diego, CA, United States) was used for statistical analysis. The method used for individual datasets is indicated in the figure legends.

ACKNOWLEDGEMENTS. Personal funding was from the Jean Shanks Pathological Society (Clinical PhD fellowship; to V.R.), CRUK UCL Centre Non-Clinical Training Awards (C416/A29287 to G.C. and CANTAC721\100022 to F.B.) and the European Commission (H2020-MSCA-IF-2018 GA: 838559; to S.C.). Research in the B.V. laboratory was supported by PTEN Research (UCL-16-001, UCL-20-001), Cancer Research UK (C23338/A25722) and the UK Biotechnology and Biological Sciences Research Council (BB/W007460/1). Research in N.R.L. laboratory was supported by PTEN Research. Research in the M.G.H.S. group was supported by Fondation ARC pour la recherche sur le cancer (ARCPJA2022060005118) and Ligue Contre le Cancer (Comité de Paris). The UCL Cancer Institute Translational Technology Platforms are supported by the CRUK UCL Centre Award (C416/A25145). The N.K. lab is funded by grants from the UK Biotechnology and Biological Sciences Research Council (BB/N009061/1) and the Wellcome Trust (108726/Z/15/Z). M.T. and K.S. are supported by PTEN Research and the NIHR Cambridge Biomedical Research Centre (NIHR203312). The PHTS Patient Registry UK is funded by PTEN Research (UOC-17-001). We thank Dr Isra Mohamed, Cambridge University NHS Foundation Trust for providing information about patient P021. We thank staff at the Technical Support Centre for Life Science Research in IMU for excellent technical support with EM processing. We also thank the UCL Research Capital Infrastructure Fund (RCIF) and the National Institute for Health Research University College London Hospitals Biomedical Research Centre for upgrade of the UCL Cancer Institute Microscopy facility and Dr Maria Whitehead and Dr Paul Elvin and members from the B.V. group for excellent feedback on the manuscript.

881 **REFERENCES**
882

883 ALIMONTI, A., CARRACEDO, A., CLOHESSY, J. G., TROTMAN, L. C., NARDELLA, C., EGIA, A., SALMENA,
884 L., SAMPIERI, K., HAVEMAN, W. J., BROGI, E., RICHARDSON, A. L., ZHANG, J. & PANDOLFI, P. P.
885 2010. Subtle variations in Pten dose determine cancer susceptibility. *Nat Genet,* 42**,** 454-8.
886 ALVAREZ-GARCIA, V., TAWIL, Y., WISE, H. M. & LESLIE, N. R. 2019. Mechanisms of PTEN loss in cancer:
887 It's all about diversity. *Semin Cancer Biol,* 59**,** 66-79.
888 ATTIA, S. M., AL-HAMAMAH, M. A., AHMAD, S. F., NADEEM, A., ATTIA, M. S. M., ANSARI, M. A.,
889 BAKHEET, S. A. & AL-AYADHI, L. Y. 2020. Evaluation of DNA repair efficiency in autistic children
890 by molecular cytogenetic analysis and transcriptome profiling. *DNA Repair (Amst),* 85**,** 102750.
891 BASSI, C., HO, J., SRIKUMAR, T., DOWLING, R. J., GORRINI, C., MILLER, S. J., MAK, T. W., NEEL, B. G.,
892 RAUGHT, B. & STAMBOLIC, V. 2013. Nuclear PTEN controls DNA repair and sensitivity to
893 genotoxic stress. *Science,* 341**,** 395-9.
894 BATEUP, H. S., JOHNSON, C. A., DENEFRIO, C. L., SAULNIER, J. L., KORNACKER, K. & SABATINI, B. L. 2013.
895 Excitatory/inhibitory synaptic imbalance leads to hippocampal hyperexcitability in mouse
896 models of tuberous sclerosis. *Neuron,* 78**,** 510-22.
897 BIRLE, D., BOTTINI, N., WILLIAMS, S., HUYNH, H., DEBELLE, I., ADAMSON, E. & MUSTELIN, T. 2002.
898 Negative feedback regulation of the tumor suppressor PTEN by phosphoinositide-induced
899 serine phosphorylation. *J Immunol,* 169**,** 286-91.
900 CASERTA, E., EGRIBOZ, O., WANG, H., MARTIN, C., KOIVISTO, C., PECOT, T., KLADNEY, R. D., SHEN, C.,
901 SHIM, K. S., PHAM, T., KARIKOMI, M. K., MAUNTEL, M. J., MAJUMDER, S., CUITINO, M. C.,
902 TANG, X., SRIVASTAVA, A., YU, L., WALLACE, J., MO, X., PARK, M., FERNANDEZ, S. A., PILARSKI,
903 R., LA PERLE, K. M., ROSOL, T. J., COPPOLA, V., CASTRILLON, D. H., TIMMERS, C., COHN, D. E.,
904 O'MALLEY, D. M., BACKES, F., SUAREZ, A. A., GOODFELLOW, P., CHAMBERLIN, H. M., MACRAE,
905 E. R., SHAPIRO, C. L., OSTROWSKI, M. C. & LEONE, G. 2015. Noncatalytic PTEN missense
906 mutation predisposes to organ-selective cancer development in vivo. *Genes Dev,* 29**,** 1707-20.
907 CHEN, C. Y., CHEN, J., HE, L. & STILES, B. L. 2018. PTEN: Tumor Suppressor and Metabolic Regulator.
908 *Front Endocrinol (Lausanne),* 9**,** 338.
909 CHEN, H. H., HANDEL, N., NGEOW, J., MULLER, J., HUHN, M., YANG, H. T., HEINDL, M., BERBERS, R. M.,
910 HEGAZY, A. N., KIONKE, J., YEHIA, L., SACK, U., BLASER, F., RENSING-EHL, A., REIFENBERGER, J.,
911 KEITH, J., TRAVIS, S., MERKENSCHLAGER, A., KIESS, W., WITTEKIND, C., WALKER, L., EHL, S.,
912 ARETZ, S., DUSTIN, M. L., ENG, C., POWRIE, F. & UHLIG, H. H. 2017. Immune dysregulation in
913 patients with PTEN hamartoma tumor syndrome: Analysis of FOXP3 regulatory T cells. *J Allergy*
914 *Clin Immunol,* 139**,** 607-620 e15.
915 CLIPPERTON-ALLEN, A. E. & PAGE, D. T. 2014. Pten haploinsufficient mice show broad brain
916 overgrowth but selective impairments in autism-relevant behavioral tests. *Hum Mol Genet,*
917 23**,** 3490-505.
918 DAVIDSON, L., MACCARIO, H., PERERA, N. M., YANG, X., SPINELLI, L., TIBAREWAL, P., GLANCY, B., GRAY,
919 A., WEIJER, C. J., DOWNES, C. P. & LESLIE, N. R. 2010. Suppression of cellular proliferation and
920 invasion by the concerted lipid and protein phosphatase activities of PTEN. *Oncogene,* 29**,** 687-
921 97.
922 DEMPSEY, D. R., VIENNET, T., IWASE, R., PARK, E., HENRIQUEZ, S., CHEN, Z., JELIAZKOV, J. R., PALANSKI,
923 B. A., PHAN, K. L., COOTE, P., GRAY, J. J., ECK, M. J., GABELLI, S. B., ARTHANARI, H. & COLE, P.
924 A. 2021. The structural basis of PTEN regulation by multi-site phosphorylation. *Nat Struct Mol*
925 *Biol,* 28**,** 858-868.
926 DI CRISTOFANO, A., DE ACETIS, M., KOFF, A., CORDON-CARDO, C. & PANDOLFI, P. P. 2001. Pten and
927 p27KIP1 cooperate in prostate cancer tumor suppression in the mouse. *Nat Genet,* 27**,** 222-4.
928 DI CRISTOFANO, A., PESCE, B., CORDON-CARDO, C. & PANDOLFI, P. P. 1998. Pten is essential for
929 embryonic development and tumour suppression. *Nat Genet,* 19**,** 348-55.

930 DICKINS, R. A., HEMANN, M. T., ZILFOU, J. T., SIMPSON, D. R., IBARRA, I., HANNON, G. J. & LOWE, S.
931 W. 2005. Probing tumor phenotypes using stable and regulated synthetic microRNA
932 precursors. *Nat Genet,* 37**,** 1289-95.
933 DRISSEN, M., VOS, J. R., COLLADO CAMPS, E., SCHUURS-HOEIJMAKERS, J. H. M., SCHIEVING, J. H. &
934 HOOGERBRUGGE, N. 2024. Increased frequency of infections and autoimmune disease in
935 adults with PTEN Hamartoma Tumour Syndrome. *Eur J Med Genet,* 70**,** 104960.
936 DROST, R. M. & JONKERS, J. 2009. Preclinical mouse models for BRCA1-associated breast cancer. *Br J*
937 *Cancer,* 101**,** 1651-7.
938 FREEMAN, D., LESCHE, R., KERTESZ, N., WANG, S., LI, G., GAO, J., GROSZER, M., MARTINEZ-DIAZ, H.,
939 ROZENGURT, N., THOMAS, G., LIU, X. & WU, H. 2006. Genetic background controls tumor
940 development in PTEN-deficient mice. *Cancer Res,* 66**,** 6492-6.
941 GARCIA-CAO, I., SONG, M. S., HOBBS, R. M., LAURENT, G., GIORGI, C., DE BOER, V. C., ANASTASIOU, D.,
942 ITO, K., SASAKI, A. T., RAMEH, L., CARRACEDO, A., VANDER HEIDEN, M. G., CANTLEY, L. C.,
943 PINTON, P., HAIGIS, M. C. & PANDOLFI, P. P. 2012. Systemic elevation of PTEN induces a tumor-
944 suppressive metabolic state. *Cell,* 149**,** 49-62.
945 GUPTA, A. & LESLIE, N. R. 2016. Controlling PTEN (Phosphatase and Tensin Homolog) Stability: A
946 DOMINANT ROLE FOR LYSINE 66. *J Biol Chem,* 291**,** 18465-73.
947 HAKEM, R., DE LA POMPA, J. L., SIRARD, C., MO, R., WOO, M., HAKEM, A., WAKEHAM, A., POTTER, J.,
948 REITMAIR, A., BILLIA, F., FIRPO, E., HUI, C. C., ROBERTS, J., ROSSANT, J. & MAK, T. W. 1996. The
949 tumor suppressor gene Brca1 is required for embryonic cellular proliferation in the mouse.
950 *Cell,* 85**,** 1009-23.
951 HAN, S. Y., KATO, H., KATO, S., SUZUKI, T., SHIBATA, H., ISHII, S., SHIIBA, K., MATSUNO, S., KANAMARU,
952 R. & ISHIOKA, C. 2000. Functional evaluation of PTEN missense mutations using in vitro
953 phosphoinositide phosphatase assay. *Cancer Res,* 60**,** 3147-51.
954 HENDRICKS, L. A. J., HOOGERBRUGGE, N., VENSELAAR, H., ARETZ, S., SPIER, I., LEGIUS, E., BREMS, H.,
955 DE PUTTER, R., CLAES, K. B. M., EVANS, D. G., WOODWARD, E. R., GENUARDI, M.,
956 BRUGNOLETTI, F., VAN IERLAND, Y., DIJKE, K., THAM, E., TESI, B., SCHUURS-HOEIJMAKERS, J.
957 H. M., BRANCHAUD, M., SALVADOR, H., JAHN, A., SCHNAITER, S., ANASTASIADOU, V. C.,
958 BRUNET, J., OLIVEIRA, C., ROHT, L., BLATNIK, A., IRMEJS, A., GROUP, P. S., MENSENKAMP, A.
959 R. & VOS, J. R. 2022. Genotype-phenotype associations in a large PTEN Hamartoma Tumor
960 Syndrome (PHTS) patient cohort. *Eur J Med Genet,* 65**,** 104632.
961 HO, J., CRUISE, E. S., DOWLING, R. J. O. & STAMBOLIC, V. 2019. PTEN Nuclear Functions. *Cold Spring*
962 *Harb Perspect Med*.
963 IGARASHI, A., ITOH, K., YAMADA, T., ADACHI, Y., KATO, T., MURATA, D., SESAKI, H. & IIJIMA, M. 2018.
964 Nuclear PTEN deficiency causes microcephaly with decreased neuronal soma size and
965 increased seizure susceptibility. *J Biol Chem,* 293**,** 9292-9300.
966 ITTMANN, M., HUANG, J., RADAELLI, E., MARTIN, P., SIGNORETTI, S., SULLIVAN, R., SIMONS, B. W.,
967 WARD, J. M., ROBINSON, B. D., CHU, G. C., LODA, M., THOMAS, G., BOROWSKY, A. & CARDIFF,
968 R. D. 2013. Animal models of human prostate cancer: the consensus report of the New York
969 meeting of the Mouse Models of Human Cancers Consortium Prostate Pathology Committee.
970 *Cancer Res,* 73**,** 2718-36.
971 JAINI, R., LOYA, M. G., KING, A. T., THACKER, S., SARN, N. B., YU, Q., STARK, G. R. & ENG, C. 2020.
972 Germline PTEN mutations are associated with a skewed peripheral immune repertoire in
973 humans and mice. *Hum Mol Genet,* 29**,** 2353-2364.
974 JUN, H. J., PAULO, J. A., APPLEMAN, V. A., YARON-BARIR, T. M., JOHNSON, J. L., YEO, A. T., ROGERS, V.
975 A., KUANG, S., VARMA, H., GYGI, S. P., TROTMAN, L. C. & CHAREST, A. 2024. Pleiotropic tumor
976 suppressive functions of PTEN missense mutations during gliomagenesis. *iScience,* 27**,** 111278.
977 KATO, T., YAMADA, T., NAKAMURA, H., IGARASHI, A., ANDERS, R. A., SESAKI, H. & IIJIMA, M. 2020. The
978 Loss of Nuclear PTEN Increases Tumorigenesis in a Preclinical Mouse Model for Hepatocellular
979 Carcinoma. *iScience,* 23**,** 101548.

980 KESSARIS, N., FOGARTY, M., IANNARELLI, P., GRIST, M., WEGNER, M. & RICHARDSON, W. D. 2006.
981 Competing waves of oligodendrocytes in the forebrain and postnatal elimination of an
982 embryonic lineage. *Nat Neurosci,* 9**,** 173-9.
983 KNOBBE, C. B., LAPIN, V., SUZUKI, A. & MAK, T. W. 2008. The roles of PTEN in development, physiology
984 and tumorigenesis in mouse models: a tissue-by-tissue survey. *Oncogene,* 27**,** 5398-415.
985 KOUGIOUMTZIDOU, E., SHIMIZU, T., HAMILTON, N. B., TOHYAMA, K., SPRENGEL, R., MONYER, H.,
986 ATTWELL, D. & RICHARDSON, W. D. 2017. Signalling through AMPA receptors on
987 oligodendrocyte precursors promotes myelination by enhancing oligodendrocyte survival.
988 *Elife,* 6.
989 KWON, C. H., LUIKART, B. W., POWELL, C. M., ZHOU, J., MATHENY, S. A., ZHANG, W., LI, Y., BAKER, S.
990 J. & PARADA, L. F. 2006. Pten regulates neuronal arborization and social interaction in mice.
991 *Neuron,* 50**,** 377-88.
992 LACHLAN, K. L., LUCASSEN, A. M., BUNYAN, D. & TEMPLE, I. K. 2007. Cowden syndrome and Bannayan
993 Riley Ruvalcaba syndrome represent one condition with variable expression and age-related
994 penetrance: results of a clinical study of PTEN mutation carriers. *J Med Genet,* 44**,** 579-85.
995 LANGDON, C. G. 2023. Nuclear PTEN's Functions in Suppressing Tumorigenesis: Implications for Rare
996 Cancers. *Biomolecules,* 13.
997 LEE, J. O., YANG, H., GEORGESCU, M. M., DI CRISTOFANO, A., MAEHAMA, T., SHI, Y., DIXON, J. E.,
998 PANDOLFI, P. & PAVLETICH, N. P. 1999. Crystal structure of the PTEN tumor suppressor:
999 implications for its phosphoinositide phosphatase activity and membrane association. *Cell,* 99**,**
1000 323-34.
1001 LEE, Y. R. & PANDOLFI, P. P. 2020. PTEN Mouse Models of Cancer Initiation and Progression. *Cold Spring*
1002 *Harb Perspect Med,* 10.
1003 LESCHE, R., GROSZER, M., GAO, J., WANG, Y., MESSING, A., SUN, H., LIU, X. & WU, H. 2002. Cre/loxP-
1004 mediated inactivation of the murine Pten tumor suppressor gene. *Genesis,* 32**,** 148-9.
1005 LESLIE, N. R. & LONGY, M. 2016. Inherited PTEN mutations and the prediction of phenotype. *Semin*
1006 *Cell Dev Biol,* 52**,** 30-8.
1007 LESLIE, N. R., MACCARIO, H., SPINELLI, L. & DAVIDSON, L. 2009. The significance of PTEN's protein
1008 phosphatase activity. *Adv Enzyme Regul,* 49**,** 190-6.
1009 LI, J., YEN, C., LIAW, D., PODSYPANINA, K., BOSE, S., WANG, S. I., PUC, J., MILIARESIS, C., RODGERS, L.,
1010 MCCOMBIE, R., BIGNER, S. H., GIOVANELLA, B. C., ITTMANN, M., TYCKO, B., HIBSHOOSH, H.,
1011 WIGLER, M. H. & PARSONS, R. 1997. PTEN, a putative protein tyrosine phosphatase gene
1012 mutated in human brain, breast, and prostate cancer. *Science,* 275**,** 1943-7.
1013 LIMA-FERNANDES, E., MISTICONE, S., BOULARAN, C., PARADIS, J. S., ENSLEN, H., ROUX, P. P., BOUVIER,
1014 M., BAILLIE, G. S., MARULLO, S. & SCOTT, M. G. 2014. A biosensor to monitor dynamic
1015 regulation and function of tumour suppressor PTEN in living cells. *Nat Commun,* 5**,** 4431.
1016 MA, J., BENITEZ, J. A., LI, J., MIKI, S., PONTE DE ALBUQUERQUE, C., GALATRO, T., ORELLANA, L., ZANCA,
1017 C., REED, R., BOYER, A., KOGA, T., VARKI, N. M., FENTON, T. R., NAGAHASHI MARIE, S. K.,
1018 LINDAHL, E., GAHMAN, T. C., SHIAU, A. K., ZHOU, H., DEGROOT, J., SULMAN, E. P., CAVENEE,
1019 W. K., KOLODNER, R. D., CHEN, C. C. & FURNARI, F. B. 2019. Inhibition of Nuclear PTEN Tyrosine
1020 Phosphorylation Enhances Glioma Radiation Sensitivity through Attenuated DNA Repair.
1021 *Cancer Cell,* 35**,** 504-518 e7.
1022 MACCARIO, H., PERERA, N. M., GRAY, A., DOWNES, C. P. & LESLIE, N. R. 2010. Ubiquitination of PTEN
1023 (phosphatase and tensin homolog) inhibits phosphatase activity and is enhanced by
1024 membrane targeting and hyperosmotic stress. *J Biol Chem,* 285**,** 12620-8.
1025 MAEHAMA, T. & DIXON, J. E. 1998. The tumor suppressor, PTEN/MMAC1, dephosphorylates the lipid
1026 second messenger, phosphatidylinositol 3,4,5-trisphosphate. *J Biol Chem,* 273**,** 13375-8.
1027 MAGNO, L., ASGARIAN, Z., PENDOLINO, V., VELONA, T., MACKINTOSH, A., LEE, F., STRYJEWSKA, A.,
1028 ZIMMER, C., GUILLEMOT, F., FARRANT, M., CLARK, B. & KESSARIS, N. 2021. Transient
1029 developmental imbalance of cortical interneuron subtypes presages long-term changes in
1030 behavior. *Cell Rep,* 35**,** 109249.

1031 MARSH, D. J., COULON, V., LUNETTA, K. L., ROCCA-SERRA, P., DAHIA, P. L., ZHENG, Z., LIAW, D., CARON,
1032 S., DUBOUE, B., LIN, A. Y., RICHARDSON, A. L., BONNETBLANC, J. M., BRESSIEUX, J. M.,
1033 CABARROT-MOREAU, A., CHOMPRET, A., DEMANGE, L., EELES, R. A., YAHANDA, A. M.,
1034 FEARON, E. R., FRICKER, J. P., GORLIN, R. J., HODGSON, S. V., HUSON, S., LACOMBE, D., ENG,
1035 C. & ET AL. 1998. Mutation spectrum and genotype-phenotype analyses in Cowden disease
1036 and Bannayan-Zonana syndrome, two hamartoma syndromes with germline PTEN mutation.
1037 *Hum Mol Genet,* 7**,** 507-15.
1038 MARSH, D. J., KUM, J. B., LUNETTA, K. L., BENNETT, M. J., GORLIN, R. J., AHMED, S. F., BODURTHA, J.,
1039 CROWE, C., CURTIS, M. A., DASOUKI, M., DUNN, T., FEIT, H., GERAGHTY, M. T., GRAHAM, J. M.,
1040 JR., HODGSON, S. V., HUNTER, A., KORF, B. R., MANCHESTER, D., MIESFELDT, S., MURDAY, V.
1041 A., NATHANSON, K. L., PARISI, M., POBER, B., ROMANO, C., ENG, C. & ET AL. 1999. PTEN
1042 mutation spectrum and genotype-phenotype correlations in Bannayan-Riley-Ruvalcaba
1043 syndrome suggest a single entity with Cowden syndrome. *Hum Mol Genet,* 8**,** 1461-72.
1044 MASSON, G. R., BURKE, J. E. & WILLIAMS, R. L. 2016a. Methods in the Study of PTEN Structure: X-Ray
1045 Crystallography and Hydrogen Deuterium Exchange Mass Spectrometry. *Methods Mol Biol,*
1046 1388**,** 215-30.
1047 MASSON, G. R., PERISIC, O., BURKE, J. E. & WILLIAMS, R. L. 2016b. The intrinsically disordered tails of
1048 PTEN and PTEN-L have distinct roles in regulating substrate specificity and membrane activity.
1049 *Biochem J,* 473**,** 135-44.
1050 MATOS-RODRIGUES, G., MARTINI, E. & LOPEZ, B. S. 2021. Mouse Models for Deciphering the Impact
1051 of Homologous Recombination on Tumorigenesis. *Cancers (Basel),* 13.
1052 MENDES-PEREIRA, A. M., MARTIN, S. A., BROUGH, R., MCCARTHY, A., TAYLOR, J. R., KIM, J. S.,
1053 WALDMAN, T., LORD, C. J. & ASHWORTH, A. 2009. Synthetic lethal targeting of PTEN mutant
1054 cells with PARP inhibitors. *EMBO Mol Med,* 1**,** 315-22.
1055 MESTER, J. L., TILOT, A. K., RYBICKI, L. A., FRAZIER, T. W., 2ND & ENG, C. 2011. Analysis of prevalence
1056 and degree of macrocephaly in patients with germline PTEN mutations and of brain weight in
1057 Pten knock-in murine model. *Eur J Hum Genet,* 19**,** 763-8.
1058 MIGHELL, T. L., EVANS-DUTSON, S. & O'ROAK, B. J. 2018. A Saturation Mutagenesis Approach to
1059 Understanding PTEN Lipid Phosphatase Activity and Genotype-Phenotype Relationships. *Am J*
1060 *Hum Genet,* 102**,** 943-955.
1061 MISTICONE, S., LIMA-FERNANDES, E. & SCOTT, M. G. 2016. Rapid Detection of Dynamic PTEN
1062 Regulation in Living Cells Using Intramolecular BRET. *Methods Mol Biol,* 1388**,** 95-110.
1063 MYERS, M. P., PASS, I., BATTY, I. H., VAN DER KAAY, J., STOLAROV, J. P., HEMMINGS, B. A., WIGLER, M.
1064 H., DOWNES, C. P. & TONKS, N. K. 1998. The lipid phosphatase activity of PTEN is critical for its
1065 tumor supressor function. *Proc Natl Acad Sci U S A,* 95**,** 13513-8.
1066 NELEN, M. R., PADBERG, G. W., PEETERS, E. A., LIN, A. Y., VAN DEN HELM, B., FRANTS, R. R., COULON,
1067 V., GOLDSTEIN, A. M., VAN REEN, M. M., EASTON, D. F., EELES, R. A., HODGSEN, S., MULVIHILL,
1068 J. J., MURDAY, V. A., TUCKER, M. A., MARIMAN, E. C., STARINK, T. M., PONDER, B. A., ROPERS,
1069 H. H., KREMER, H., LONGY, M. & ENG, C. 1996. Localization of the gene for Cowden disease to
1070 chromosome 10q22-23. *Nat Genet,* 13**,** 114-6.
1071 NGEOW, J. & ENG, C. 2019. PTEN in Hereditary and Sporadic Cancer. *Cold Spring Harb Perspect Med*.
1072 ODRIOZOLA, L., SINGH, G., HOANG, T. & CHAN, A. M. 2007. Regulation of PTEN activity by its carboxyl-
1073 terminal autoinhibitory domain. *J Biol Chem,* 282**,** 23306-15.
1074 OOMS, L. M., BINGE, L. C., DAVIES, E. M., RAHMAN, P., CONWAY, J. R., GURUNG, R., FERGUSON, D. T.,
1075 PAPA, A., FEDELE, C. G., VIEUSSEUX, J. L., CHAI, R. C., KOENTGEN, F., PRICE, J. T., TIGANIS, T.,
1076 TIMPSON, P., MCLEAN, C. A. & MITCHELL, C. A. 2015. The Inositol Polyphosphate 5-
1077 Phosphatase PIPP Regulates AKT1-Dependent Breast Cancer Growth and Metastasis. *Cancer*
1078 *Cell,* 28**,** 155-69.
1079 PAL, A., BARBER, T. M., VAN DE BUNT, M., RUDGE, S. A., ZHANG, Q., LACHLAN, K. L., COOPER, N. S.,
1080 LINDEN, H., LEVY, J. C., WAKELAM, M. J., WALKER, L., KARPE, F. & GLOYN, A. L. 2012. PTEN

1081 mutations as a cause of constitutive insulin sensitivity and obesity. *N Engl J Med,* 367**,** 1002-
1082 11.
1083 PODSYPANINA, K., ELLENSON, L. H., NEMES, A., GU, J., TAMURA, M., YAMADA, K. M., CORDON-CARDO,
1084 C., CATORETTI, G., FISHER, P. E. & PARSONS, R. 1999. Mutation of Pten/Mmac1 in mice causes
1085 neoplasia in multiple organ systems. *Proc Natl Acad Sci U S A,* 96**,** 1563-8.
1086 POST, K. L., BELMADANI, M., GANGULY, P., MEILI, F., DINGWALL, R., MCDIARMID, T. A., MEYERS, W.
1087 M., HERRINGTON, C., YOUNG, B. P., CALLAGHAN, D. B., ROGIC, S., EDWARDS, M.,
1088 NICIFOROVIC, A., CAU, A., RANKIN, C. H., O'CONNOR, T. P., BAMJI, S. X., LOEWEN, C. J. R.,
1089 ALLAN, D. W., PAVLIDIS, P. & HAAS, K. 2020. Multi-model functionalization of disease-
1090 associated PTEN missense mutations identifies multiple molecular mechanisms underlying
1091 protein dysfunction. *Nat Commun,* 11**,** 2073.
1092 RANTAKARI, P., NIKKILA, J., JOKELA, H., OLA, R., PYLKAS, K., LAGERBOHM, H., SAINIO, K., POUTANEN,
1093 M. & WINQVIST, R. 2010. Inactivation of Palb2 gene leads to mesoderm differentiation defect
1094 and early embryonic lethality in mice. *Hum Mol Genet,* 19**,** 3021-9.
1095 ROY, R., CHUN, J. & POWELL, S. N. 2011. BRCA1 and BRCA2: different roles in a common pathway of
1096 genome protection. *Nat Rev Cancer,* 12**,** 68-78.
1097 SCHEI-ANDERSEN, A. J., WITJES, V. M., VOS, J. R., MENSENKAMP, A. R., VAN ALTENA, A., SCHIEVING,
1098 J., SIMONS, M., SCHUURS-HOEIJMAKERS, J. H. M., GROUP, P. S. & HOOGERBRUGGE, N. 2025.
1099 Non-serous ovarian cancer in PTEN Hamartoma Tumor Syndrome: additional evidence for
1100 increased risk. *Fam Cancer,* 24**,** 28.
1101 SCHONHUBER, N., SEIDLER, B., SCHUCK, K., VELTKAMP, C., SCHACHTLER, C., ZUKOWSKA, M., ESER, S.,
1102 FEYERABEND, T. B., PAUL, M. C., ESER, P., KLEIN, S., LOWY, A. M., BANERJEE, R., YANG, F., LEE,
1103 C. L., MODING, E. J., KIRSCH, D. G., SCHEIDELER, A., ALESSI, D. R., VARELA, I., BRADLEY, A., KIND,
1104 A., SCHNIEKE, A. E., RODEWALD, H. R., RAD, R., SCHMID, R. M., SCHNEIDER, G. & SAUR, D.
1105 2014. A next-generation dual-recombinase system for time- and host-specific targeting of
1106 pancreatic cancer. *Nat Med,* 20**,** 1340-1347.
1107 SCUDAMORE, C. 2014. Practical approaches to reviewing and recording pathology data. *In:* C.L., S. (ed.)
1108 *A Practical Guide to Histology of the Mouse* Chichester, UK: Wiley-Blackwell.
1109 SHEN, W. H., BALAJEE, A. S., WANG, J., WU, H., ENG, C., PANDOLFI, P. P. & YIN, Y. 2007. Essential role
1110 for nuclear PTEN in maintaining chromosomal integrity. *Cell,* 128**,** 157-70.
1111 SMITH, I. N. & BRIGGS, J. M. 2016. Structural mutation analysis of PTEN and its genotype-phenotype
1112 correlations in endometriosis and cancer. *Proteins,* 84**,** 1625-1643.
1113 SPINELLI, L., BLACK, F. M., BERG, J. N., EICKHOLT, B. J. & LESLIE, N. R. 2015. Functionally distinct groups
1114 of inherited PTEN mutations in autism and tumour syndromes. *J Med Genet,* 52**,** 128-34.
1115 STECK, P. A., PERSHOUSE, M. A., JASSER, S. A., YUNG, W. K., LIN, H., LIGON, A. H., LANGFORD, L. A.,
1116 BAUMGARD, M. L., HATTIER, T., DAVIS, T., FRYE, C., HU, R., SWEDLUND, B., TENG, D. H. &
1117 TAVTIGIAN, S. V. 1997. Identification of a candidate tumour suppressor gene, MMAC1, at
1118 chromosome 10q23.3 that is mutated in multiple advanced cancers. *Nat Genet,* 15**,** 356-62.
1119 SUZUKI, A., DE LA POMPA, J. L., STAMBOLIC, V., ELIA, A. J., SASAKI, T., DEL BARCO BARRANTES, I., HO,
1120 A., WAKEHAM, A., ITIE, A., KHOO, W., FUKUMOTO, M. & MAK, T. W. 1998. High cancer
1121 susceptibility and embryonic lethality associated with mutation of the PTEN tumor suppressor
1122 gene in mice. *Curr Biol,* 8**,** 1169-78.
1123 TIBAREWAL, P., RATHBONE, V., CONSTANTINOU, G., PEARCE, W., ADIL, M., VARYOVA, Z., FOLKES, L.,
1124 HAMPSON, A., CLASSEN, G. A. E., ALVES, A., CARVALHO, S., SCUDAMORE, C. L. &
1125 VANHAESEBROECK, B. 2022. Long-term treatment of cancer-prone germline PTEN mutant
1126 mice with low-dose rapamycin extends lifespan and delays tumour development. *J Pathol,*
1127 258**,** 382-394.
1128 TIBAREWAL, P., ZILIDIS, G., SPINELLI, L., SCHURCH, N., MACCARIO, H., GRAY, A., PERERA, N. M.,
1129 DAVIDSON, L., BARTON, G. J. & LESLIE, N. R. 2012. PTEN protein phosphatase activity
1130 correlates with control of gene expression and invasion, a tumor-suppressing phenotype, but
1131 not with AKT activity. *Sci Signal,* 5**,** ra18.

1132 TILOT, A. K., GAUGLER, M. K., YU, Q., ROMIGH, T., YU, W., MILLER, R. H., FRAZIER, T. W., 2ND & ENG,
1133 C. 2014. Germline disruption of Pten localization causes enhanced sex-dependent social
1134 motivation and increased glial production. *Hum Mol Genet,* 23**,** 3212-27.
1135 TORRES, J. & PULIDO, R. 2001. The tumor suppressor PTEN is phosphorylated by the protein kinase
1136 CK2 at its C terminus. Implications for PTEN stability to proteasome-mediated degradation. *J*
1137 *Biol Chem,* 276**,** 993-8.
1138 TSUZUKI, T., FUJII, Y., SAKUMI, K., TOMINAGA, Y., NAKAO, K., SEKIGUCHI, M., MATSUSHIRO, A.,
1139 YOSHIMURA, Y. & MORITAT 1996. Targeted disruption of the Rad51 gene leads to lethality in
1140 embryonic mice. *Proc Natl Acad Sci U S A,* 93**,** 6236-40.
1141 VAZQUEZ, F., GROSSMAN, S. R., TAKAHASHI, Y., ROKAS, M. V., NAKAMURA, N. & SELLERS, W. R. 2001.
1142 Phosphorylation of the PTEN tail acts as an inhibitory switch by preventing its recruitment into
1143 a protein complex. *J Biol Chem,* 276**,** 48627-30.
1144 WANG, M., WEI, P. C., LIM, C. K., GALLINA, I. S., MARSHALL, S., MARCHETTO, M. C., ALT, F. W. & GAGE,
1145 F. H. 2020. Increased Neural Progenitor Proliferation in a hiPSC Model of Autism Induces
1146 Replication Stress-Associated Genome Instability. *Cell Stem Cell,* 26**,** 221-233 e6.
1147 WEI, R., HITOMI, M., SADLER, T., YEHIA, L., CALVETTI, D., SCOTT, J. & ENG, C. 2024. Quantitative
1148 evaluation of DNA damage repair dynamics to elucidate predictors of autism vs. cancer in
1149 individuals with germline PTEN variants. *PLoS Comput Biol,* 20**,** e1012449.
1150 WHITE, S. L., JAMIL, T., BELL, C., FISHBEIN, L., HAUGEN, B. R., GIGNOUX, C. R. & POZDEYEV, N. 2025.
1151 Population Prevalence of the Major Thyroid Cancer–Associated Syndromes. *The Journal of*
1152 *Clinical Endocrinology & Metabolism*.
1153 YAN, D. H., WEN, Y., SU, L. K., XIA, W., WANG, S. C., ZHANG, S., GAN, L., LEE, D. F., SPOHN, B., FREY, J.
1154 A., HORTOBAGYI, G. N. & HUNG, M. C. 2004. A delayed chemically induced tumorigenesis in
1155 Brca2 mutant mice. *Oncogene,* 23**,** 1896-901.
1156 YEHIA, L. & ENG, C. 2018. 65 YEARS OF THE DOUBLE HELIX: One gene, many endocrine and metabolic
1157 syndromes: PTEN-opathies and precision medicine. *Endocr Relat Cancer,* 25**,** T121-T140.
1158 YEHIA, L., KEEL, E. & ENG, C. 2020. The Clinical Spectrum of PTEN Mutations. *Annu Rev Med,* 71**,** 103-
1159 116.
1160 YEHIA, L., NGEOW, J. & ENG, C. 2019. PTEN-opathies: from biological insights to evidence-based
1161 precision medicine. *J Clin Invest,* 129**,** 452-464.
1162 YIP, H. Y. K., CHEE, A., ANG, C. S., SHIN, S. Y., OOMS, L. M., MOHAMMADI, Z., PHILLIPS, W. A., DALY, R.
1163 J., COLE, T. J., BRONSON, R. T., NGUYEN, L. K., TIGANIS, T., HOBBS, R. M., MCLEAN, C. A.,
1164 MITCHELL, C. A. & PAPA, A. 2020. Control of Glucocorticoid Receptor Levels by PTEN
1165 Establishes a Failsafe Mechanism for Tumor Suppression. *Mol Cell,* 80**,** 279-295 e8.
1166 YUAN, E., TSAI, P. T., GREENE-COLOZZI, E., SAHIN, M., KWIATKOWSKI, D. J. & MALINOWSKA, I. A. 2012.
1167 Graded loss of tuberin in an allelic series of brain models of TSC correlates with survival, and
1168 biochemical, histological and behavioral features. *Hum Mol Genet,* 21**,** 4286-300.
1169 ZHOU, J., BLUNDELL, J., OGAWA, S., KWON, C. H., ZHANG, W., SINTON, C., POWELL, C. M. & PARADA,
1170 L. F. 2009. Pharmacological inhibition of mTORC1 suppresses anatomical, cellular, and
1171 behavioral abnormalities in neural-specific Pten knock-out mice. *J Neurosci,* 29**,** 1773-83.

1172
1173

1174

1175 **Table 1**

		PHTS patients with *PTEN* R173 variants	PHTS patients with other nuclear excluded *PTEN* variants	Both groups combined
Patient demographics	Number of patients (N)	34	25	59
	Age range (median age)	7mo-63y (12.5y)	1y-40y (6y)	7mo-63y (10y)
	Gender distribution N (%)	m: 19 (56%) f: 14 (41%) NR: 1 (3%)	m: 12 (48%) m: 9 (36%) NR: 4 (16%)	m: 31(52%) f: 23 (39%) NR: 5 (8%)
Phenotypes (N (%))				
Neuro-developmental	Macrocephaly	32 (94%)	21 (84%)	53 (90%)
	Developmental disorders	18 (53%)	16 (64%)	34 (58%)
Cutaneous and vascular features	Cutaneous pathology	16 (47%)	12 (48%)	28 (47%)
	Vascular abnormalities	5 (15%)	3 (12%)	8 (14%)
	Lipomas	-	4 (16%)	4 (7%)
	Malignant cancer of skin	1 (3%) Age: 63y	-	1 (1.7 %)
Immune/Lymphoid features	Various	3 (9%)	1 (4%)	4 (7%)
Thyroid	Benign lesions	6 (18%)	4 (16%)	10 (17%)
	Malignant cancer	1 (3%) Age: 59y	1 (4%) 29y	2 (3%)
Gastro-intestinal	Benign polyps	4 (12%)	5 (20%)	9 (15%)
Breast	Benign lesions	2 (6%)	1 (4%)	3 (5%)
	Malignant cancer	2 (6%) Ages: 54y & 59y	-	2 (3%)
Ovary	Benign lesions	3 (9%)	-	3 (5%)
	Malignant cancer	1 (3%) Age: 63y	-	1 (1.7 %)
Uterus	Benign lesions	3 (9%)	-	3 (5%)
Other cancers	Testicular cancer	-	1 (4%) Age: 29y	1 (1.7%)
	Lung cancer	-	1 (4%) Age: NR	1 (1.7%)

1176

1177 **Table 1. Clinical phenotypes of PHTS patients with *Pten-R173* variants and other nuclear excluded**
1178 ***Pten* variants**

1179 mo, age in months; y, age in years; m, males; f, females, NR, not recorded. Phenotypic categories
1180 include the following: Developmental disorders; global developmental delay, delay in speech
1181 development, mental retardation, autism spectrum disorder, special educational needs. Cutaneous
1182 pathology; hamartomas, tricholemmoma, mucocutaneous lesions, acral keratoses, palmoplantar
1183 keratoses, oral papillomas, penile freckling, facial papules, café-au-lait spots, skin tags. Vascular
1184 abnormalities; haemangiomas, venous malformations, arterio-venous malformations. Immune/

1185 lymphoid features; recurrent upper respiratory tract infections, hypogammaglobulinemia, enlarged
1186 tonsils and adenoids, lymphadenopathy, splenomegaly. Thyroid benign lesions; cyst, nodules,
1187 adenomas. Thyroid malignant cancer; follicular cancer, papillary-follicular thyroid cancer. Breast
1188 benign lesions; fibrocystic disease of the breast, fibroadenomas, benign breast disease. Breast
1189 malignant cancer; ductal breast carcinoma, invasive ductal carcinoma and ductal carcinoma in-situ of
1190 the breast. Ovary benign lesions; ovarian cysts, benign neoplasm. Ovary malignant cancer; malignant
1191 neoplasm of the ovary. Uterus benign lesions; uterine fibroids, endometrial polyp. The phenotypes of
1192 individual patients are listed in Supplementary Tables 1 and 2.
1193

1194 **Table 2**

1195

Phenotypes	Mouse genotype				
	***Pten*$^{+R173C}$**	***Pten*$^{+/-}$**	***Pten*$^{-/-}$**	***Pten*$^{+/m3m4}$**	***Pten*$^{m3m4/m3m4}$**
Increased brain size	Yes	Yes	ND	Yes	Yes
Bigger corpus callosum	Yes	Yes	ND	ND	ND
Increased numbers of oligodendroglia cells	Yes	No	ND	No	Yes
Astrogliosis	No	No	ND	No	Yes
Increased cell body size	Yes	No	Yes	No	Yes
Increased neuronal complexity	Yes	No	Yes	No	No
Enlarged axons	Yes	No	ND	ND	ND
thinner myelin	Yes	Yes	ND	ND	ND
Sociability	No significant difference	ND	ND	No significant difference	Too social with revised criteria
Motor coordination	ND	ND	ND	ND	reduced
Locomotion	reduced	ND	ND	ND	ND

1196

1197 **Table 2. Neuronal and behavioural phenotypes in mice with *Pten* mutations**: Table shows data from
1198 *Pten*$^{+/R173C}$, *Pten*$^{+/-}$, and conditional *Pten*$^{-/-}$ mice from this study, and *Pten*$^{+/m3m4}$ *and* Pten$^{m3m4/m3m4}$ mice
1199 as reported in (Mester et al., 2011, Tilot et al., 2014). ND; not determined. The behavioural assays
1200 (sociability, motor coordination and locomotion) are relative to wild type littermate mice.

1201
1202

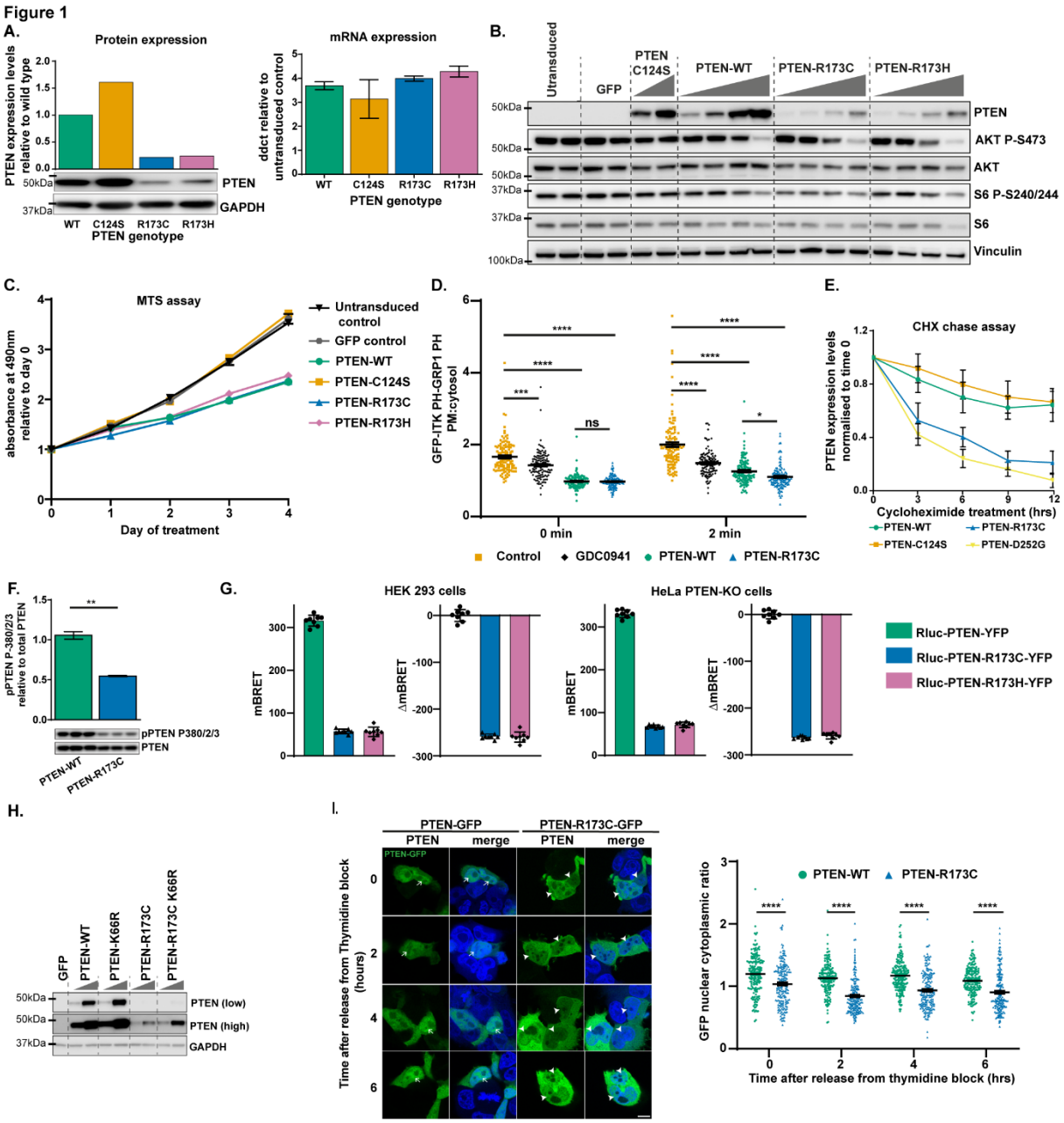

Figure 1. Characterisation of PTEN-R173C/H. (**A-C**) Transient lentiviral expression in U87 cells of PTEN-WT or the indicated PTEN mutants at fixed (A and C) or increasing concentrations of lentiviral particles (B). 48 h after transduction (A and B), cells were either lysed and PTEN expression and (B) AKT P-S473 and S6 P-S240/244 assessed by immunoblotting, or (A) qPCR analysis was performed to determine PTEN mRNA levels (mean ± SEM, n=3, right panel). The PTEN-C124S mutant was used as a control. (**C**) Cell proliferation was determined by MTS assay over 4 days. Graph shows the mean ± SEM of absorbance at 490 nm relative to day 0 from 10 replicate wells of a representative experiment from n=2. Immunoblots of PTEN protein and AKT P-S473 from the cells in (C) are shown in **Fig. S2A**. (**D**) U87 cells transduced with lentivirus expressing a PIP_3 biosensor, with or without PTEN-WT or PTEN-R173C, were pre-treated ± GDC-0941 (1 µM) for 1 h, followed ± insulin treatment (100 nM) for 2 min. The cells were stained with antibodies to PTEN and imaged by confocal microscopy (images in **Fig. S2B**). Graph shows mean fluorescence intensity (MFI) of the PIP_3 biosensor at the plasma membrane normalized to the MFI of the PIP_3 biosensor in the cytosol. Data shown as mean ± SEM from 3 independent experiments, statistical analysis performed using 2-way ANOVA. Representative immunoblots for PTEN protein and AKT P-S473 from the cells are shown in **Fig. S2C**. (**E-F**) Transient lentiviral expression

1220 of PTEN wild-type (WT) or the indicated PTEN mutants in U87 cells. (E) The cells were treated with
1221 cycloheximide and PTEN protein expression levels determined by immunoblotting at the indicated
1222 time points. Graph shows PTEN protein levels normalized to time 0, data shown as mean ± SEM, n=6.
1223 Representative blots shown in **Fig. S3A**. (F) Phosphorylation of PTEN on S380/T382/T383 was
1224 determined by immunoblotting. Quantification shows mean ± SEM, n=3, statistical analysis was
1225 performed using Unpaired Student's t-test. (**G**) mBRET and ΔmBRET values, obtained in live HEK-293T
1226 and HeLa PTEN KO cells, transfected with Rluc-PTEN-WT-YFP, Rluc-PTEN-R173C-YFP or Rluc-PTEN-
1227 R173H-YFP. Graphs represent mean ± SD of n=8 points from a representative experiment from 3
1228 independent experiments. (**H**) Transient lentiviral expression of PTEN-WT or the indicated PTEN
1229 mutants in U87 cells. Protein extracts from these cells were used for immunoblotting to assess PTEN
1230 protein levels. (**I**) Lenti-X™ 293T cells expressing GFP-tagged PTEN-WT or PTEN-R173C were arrested
1231 in the G1/S phase of cell cycle by double-thymidine block and imaged by confocal microscopy at the
1232 indicated time points after release from thymidine block, for expression of PTEN-GFP. Left panel shows
1233 representative images, arrows indicate nuclear PTEN-WT or reduced nuclear PTEN-R173C. Scale bar:
1234 10 µm. The graph shows the nuclear:cytoplasmic ratio of the mean fluorescence intensity (MFI) of the
1235 PTEN-GFP signal (mean ± SEM; n=3, statistical analysis performed using 2-way ANOVA). p-values for
1236 all statistical tests: *, $p< 0.05$; **, $p<0.01$; ***, $p<0.001$; ****, $p<0.0001$.

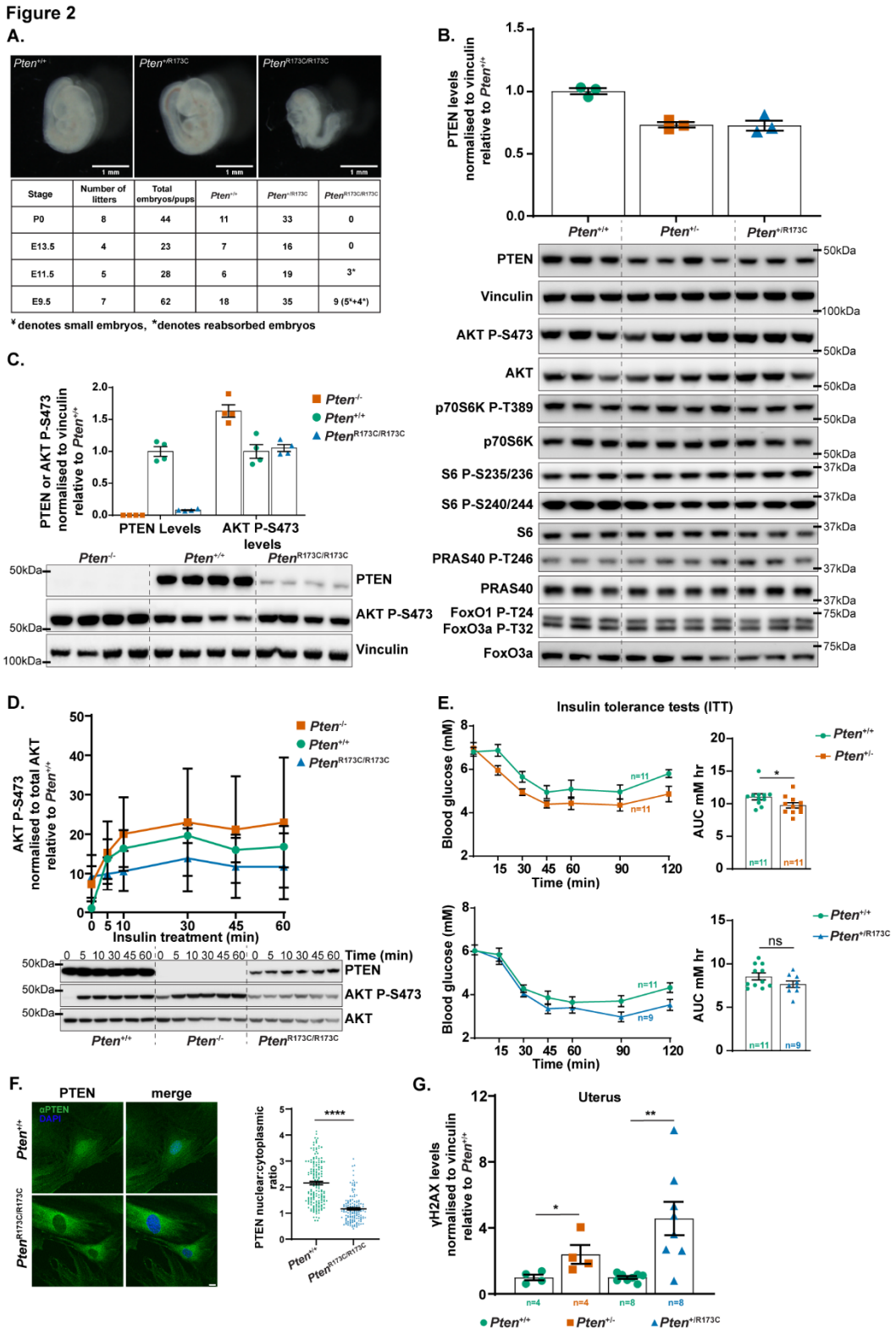

Figure 2. Characterisation of *Pten*$^{+/R173C}$ mice. (**A**) Homozygous *Pten*$^{R173C/R173C}$ mice die *in utero* after embryonic stage E9.5. Images show morphology of E9.5 *Pten*$^{+/+}$, *Pten*$^{+/R173C}$ and *Pten*$^{R173C/R173C}$ embryos. Scale bar: 1 mm. The table shows the number of embryos/pups of each genotype obtained at the indicated time points. ¥ indicates embryos smaller in size and * indicates embryos that had been reabsorbed. (**B, C**) Protein extracts from MEFs of the indicated genotype were used for immunoblotting with the antibodies shown. Data shown as mean ± SEM. At least 3 independent MEF lines of each were used for (B) and 2 independent MEF lines were used for (C). (**D**) MEFs of the

1246 indicated genotype were treated with insulin (100 nM) for the indicated times and protein extracts
1247 immunoblotted with the antibodies shown. Data shown as mean ± SEM from 2 independent MEF lines
1248 for each genotype. (**E**) ITT assays on 3-month-old male mice of the indicated genotypes. XY curves
1249 show blood glucose levels post insulin injection over time. Bar graphs show mean ± SEM of
1250 measurements of Area Under the Curve (AUC). Statistical analysis performed using Unpaired Student's
1251 t-test. (**F**) MEFs of the indicated genotype were immunostained with antibodies to PTEN (green) and
1252 DAPI (blue) and imaged by confocal microscopy. Scale bar: 10 µm. Graphs show nuclear:cytoplasmic
1253 ratio of the GFP MFI (mean ± SEM from 3 independent experiments). Statistical analysis was performed
1254 using Unpaired Student's t-test. (**G**) 6-week-old mice of the indicated genotypes were treated with
1255 7Gy γ-radiation and protein extracts from uterus were used for immunoblotting. Graph shows levels
1256 of γH2AX relative to littermate *Pten*$^{+/+}$ controls. Data shown as mean ± SEM. Statistical analysis was
1257 performed using Mann–Whitney U tests. Accompanying immunoblots are shown in **Fig. S9A**. p-values
1258 for all statistical analysis: *, $p< 0.05$; **, $p<0.01$; ***, $p<0.001$; ****, $p<0.0001$. Mice used for
1259 generating MEF lines in (A-D and F) and for experiments in (E and G) were on a C57BL/6J background.

Figure 3

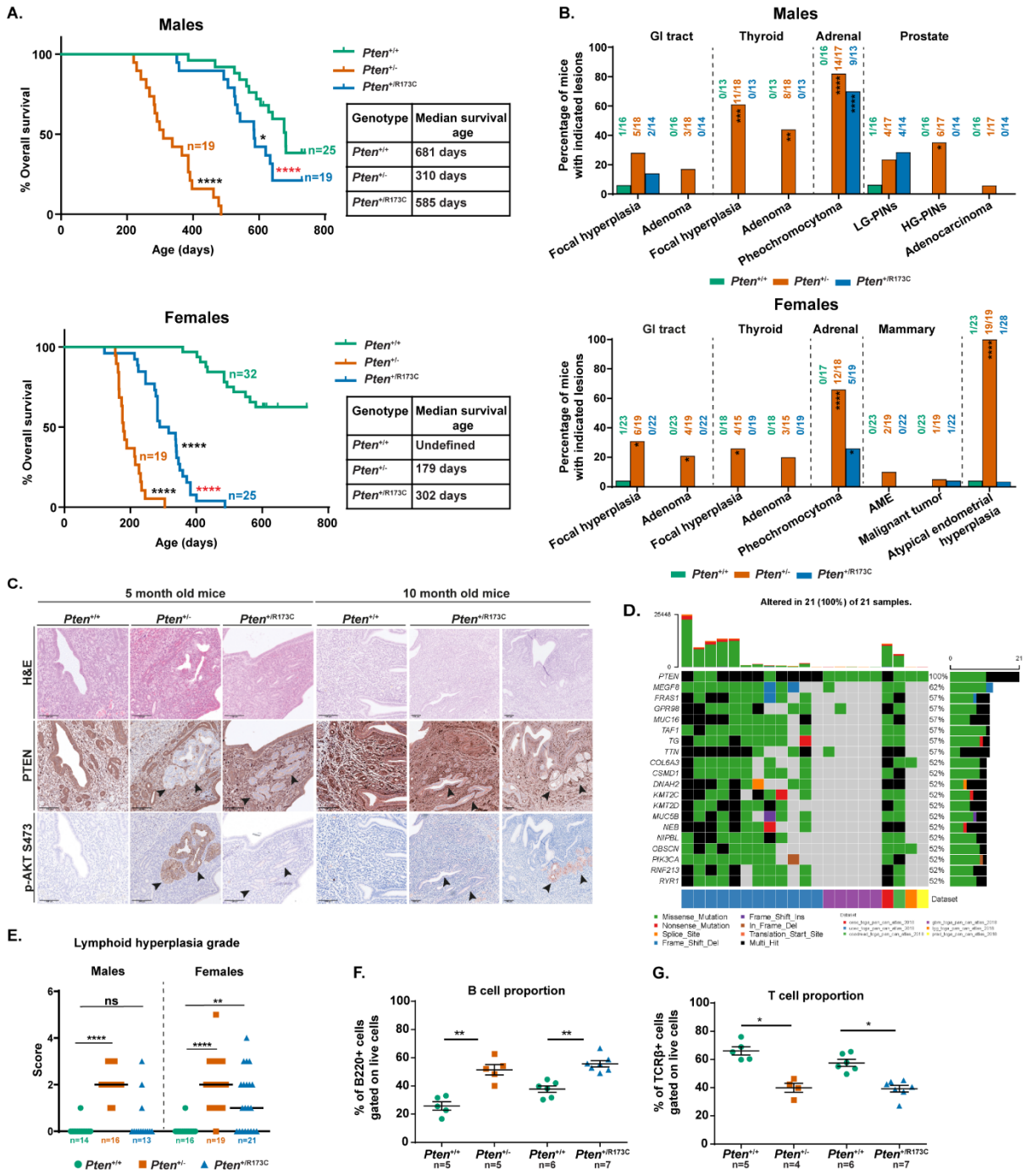

Figure 3. Survival and histopathological analysis of *Pten*$^{+/R173C}$ mice. *Pten*$^{+/R173C}$ and *Pten*$^{+/-}$ mice on a mixed C57BL/6J x Sv129 background were allowed to age. Mice were euthanized for welfare reasons (ill health or palpable masses with a combined size of ≥ 1.4 cm^2 surface area) or at a specified age. (**A**) Kaplan–Meier survival curves for male and female mice. Statistical analysis was performed using Log-rank (Mantel–Cox) test and Gehan–Breslow–Wilcoxon test. Comparisons were made to *Pten*$^{+/+}$ mice (p-values shown as black stars) or *Pten*$^{+/-}$ mice (p-values shown as red stars). Table show median survival age of the mice. (**B**) Incidence of specific tumour types in male and female mice, as assessed by histopathological analysis on all mice. Statistical analysis was performed using Fisher's exact test. (**C**) Representative IHC images of uteri from female *Pten*$^{+/R173C}$ and *Pten*$^{+/-}$ and littermate *Pten*$^{+/+}$ controls at the indicated timepoints, black arrowheads indicate loss of PTEN immunoreactivity and the corresponding AKT P-S473 immunoreactivity. (**D**) Oncoplot showing co-occurrence of mutations in the

1273 indicated genes in tumor samples harbouring PTEN-R173C mutation (cBioportal). (**E**) Grade of
1274 lymphoid hyperplasia in mice at the end of study. Graph shows scatter plot of scores from individual
1275 mice with line at median score. Statistical analysis was performed using Fisher's exact test. (**F-G**) Flow
1276 cytometry analysis was performed on the lymph nodes of female *Pten*$^{+/R173C}$, *Pten*$^{+/-}$ and littermate
1277 *Pten*$^{+/+}$ controls at 5 and 10 months of age. Graphs show the proportion of (F) B220+ B-cells and (G)
1278 TCRβ+ T-cells. Statistical analysis was performed using Mann–Whitney U test. p-values for all statistical
1279 analysis: *, $p< 0.05$; **, $p<0.01$; ***, $p<0.001$; ****, $p<0.0001$.

Figure 4

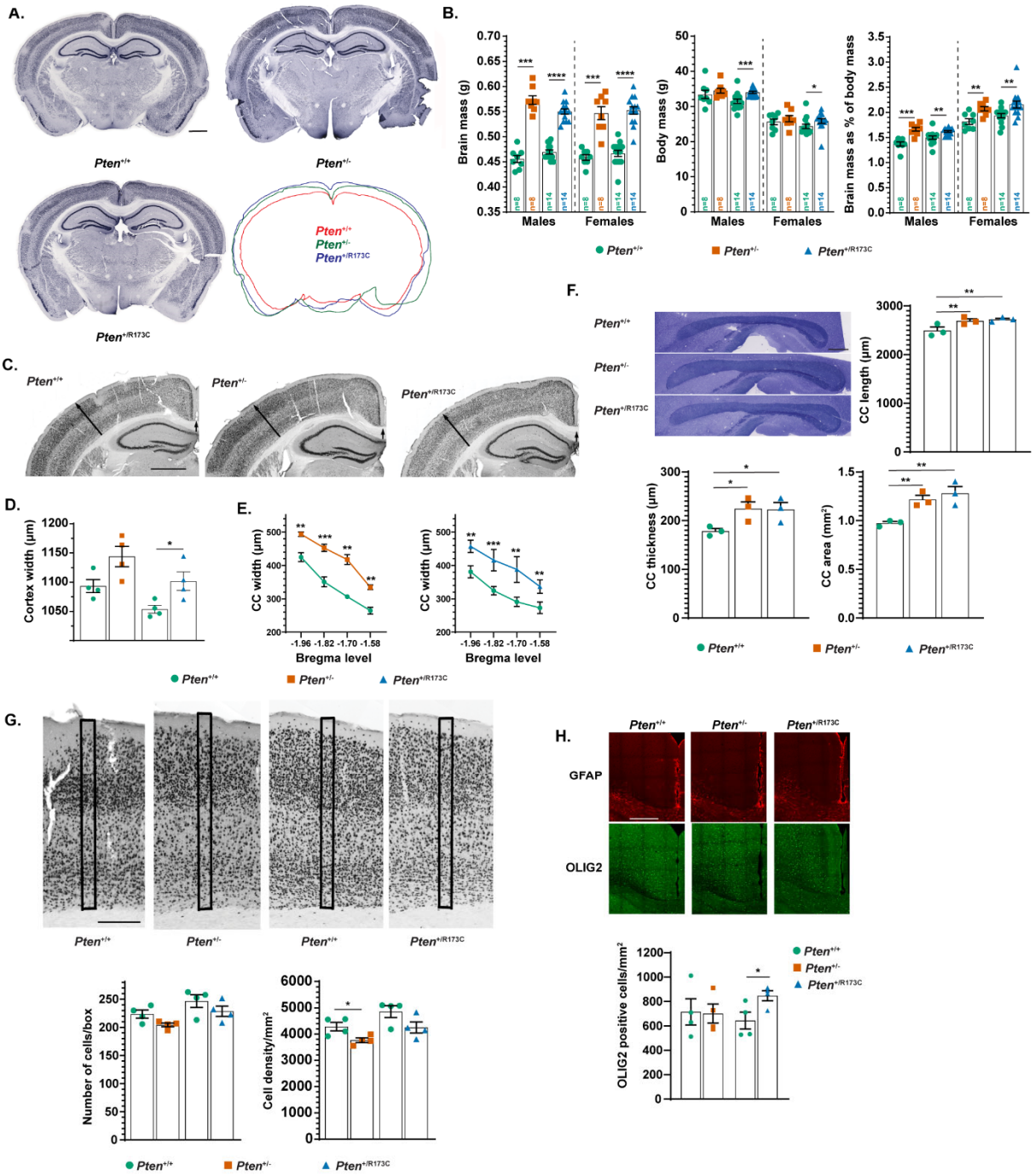

Figure 4. Enlarged brain phenotype with associated increases in grey and white matter areas in *Pten* mutant mice. (**A**) Representative NeuN immunostaining of coronal sections from *Pten*$^{+/+}$ and mutant animals at 3 months. The overlay of the contours of the depicted slices is also shown. Scale bar: 1000 µm. (**B**) Brain mass, body mass and brain mass as a % of body mass for male and female *Pten*$^{+/-}$, *Pten*$^{+/R173C}$ and WT littermate controls at 3 months. Data show mean ± SEM, statistical analysis performed using Two-tailed Mann-Whitney U test. (**C**) Representative NeuN immunostaining from coronal sections of WT and mutant animals at 3 months. Scale bar: 1000 µm. (**D**) Quantification of cortical thickness in the primary somatosensory cortex barrel field (area indicated with long arrows in C). n = 4 mice of each sex and genotype. Data show mean ± SEM, statistical analysis performed using Two-tailed Unpaired Student's t-test. (**E**) Quantification of the thickness of the corpus callosum at the indicated Bregma levels (area indicated with short arrows in C). n=4 mice of each sex and genotype.

Data show mean ± SEM, statistical analysis performed using Two-way RM ANOVA with uncorrected Fisher's LSD test. (**F**) Representative sagittal sections from control and mutant mouse brains stained with Toluidine Blue and quantification of the corpus callosum length, thickness, and area. Scale bar: 500 µm. n=3 mice per genotype. Data show mean ± SEM, statistical analysis performed using One-way RM ANOVA with uncorrected Fisher's LSD test. (**G**) Top: Representative images of coronal sections from the somatosensory cortex of *Pten*$^{+/+}$ and mutant animals at 3 months stained for NeuN. Scale bar: 250 µm. Bottom: Quantification of the number and density of neurons in the indicated boxed areas in (G). n=4 mice of each sex each genotype. Data show mean ± SEM; statistical analysis performed using Two-tailed Unpaired Student's t-test. (**H**) Top: Representative images of sections from *Pten*$^{+/+}$ and *Pten* mutant animals at 3 months immunostained with OLIG2 and GFAP, Scale bar: 100 µm, and bottom: quantification of OLIG2 positive cells in the motor cortex. n=4 mice per genotype. Data show mean ± SEM and statistical analysis performed using Two-tailed Unpaired Student's t-test. p-values for all statistical tests: *, $p<0.05$; **, $p<0.01$; ***, $p<0.001$; ****, $p<0.0001$. Mice used were on a mixed C57BL/6J x Sv129 background.

Figure 5

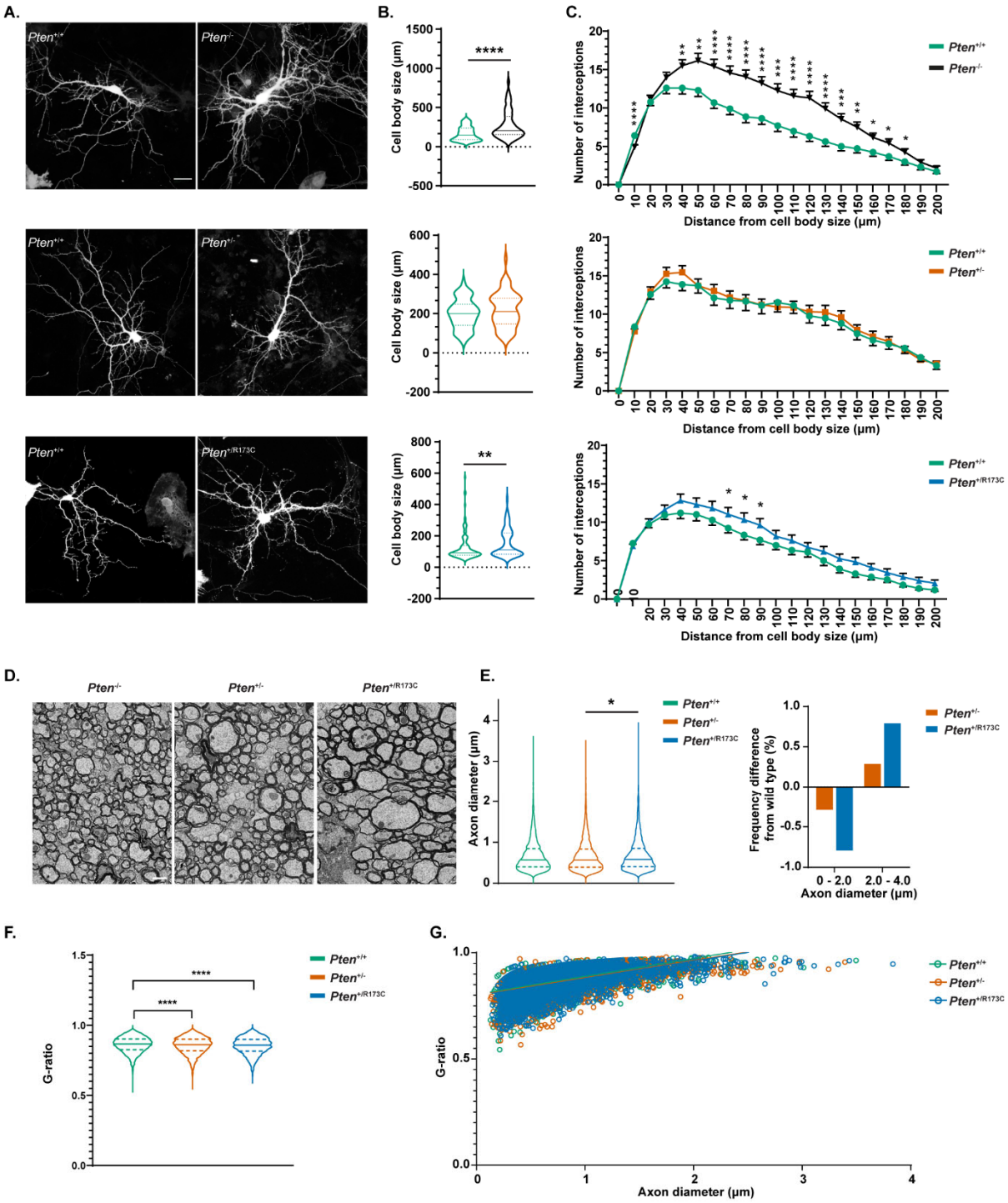

Figure 5. Neuronal and glial deficits in *Pten*$^{+/R173C}$ and *Pten*$^{+/-}$ mice. (**A**) Representative images from GFP-transfected cortico-hippocampal neurons prepared from the indicated *Pten* mutants and their respective *Pten*$^{+/+}$ littermate controls at DIV12/13. Neurons were stained for GFP. Scale bar: 20 µm. (**B**) Quantification of cell body size of GFP-transfected cultured cortico-hippocampal neurons shown in (A). from n>60 cells for each genotype from 3-6 independent experiments. Violin plots show mean ± SEM, statistical analysis performed using Two-tailed Mann-Whitney U test. (**C**) Sholl analysis of GFP-transfected cortico-hippocampal neurons shown in (A) from n=63–122 cells from 3–5 independent experiments. Data show mean ± SEM, statistical analysis performed using Two-way RM ANOVA with uncorrected Fisher's LSD test. (**D**) Representative electron micrographs of the corpus callosum in cross-sections from 3-month-old *Pten*$^{+/+}$, *Pten*$^{+/-}$ and *Pten*$^{+/R173C}$ mice. Scale bar: 1 µm. (**E**) Quantification of axonal dimeters and their frequency difference in mutant mice compared to *Pten*$^{+/+}$ littermate

1319 controls. >4500 axons measured in each of three mice per genotype. Violin plots indicate mean ± SEM,
1320 statistical analysis performed using Two-tailed Mann-Whitney U test. (**F**) Quantification of g-ratios for
1321 corpus callosum axons. >4500 axons measured in each of three mice per genotype. Statistical analysis
1322 performed using Two-tailed Mann-Whitney U test. (**G**) Scatter plot of g-ratios as a function of axon
1323 diameter in 3-month-old *Pten*$^{+/+}$, *Pten*$^{+/-}$ and *Pten*$^{+/R173C}$ mice. >4500 axons measured in each of three
1324 mice per genotype. p-values for all statistical tests: *, p< 0.05; **, p<0.01; ***, p<0.001; ****,
1325 p<0.0001. Mice used in (A-C) were on a C57BL/6J background, and in (D-G) were on a mixed C57BL/6J
1326 x Sv129 background.
1327